Using Remote Sensing and GIS to Identify Magmatic Strain Accommodation: The Case Study of Mt Marsabit, Kenya

A thesis submitted to the Faculty of Salem State University in partial fulfillment of the requirements for the degree of Master of Science in Geo-Information Science

Cora Van Hazinga, Salem State University

Advisors:

Dr. Sara Mana, Salem State University

Dr. James Muirhead, University of Auckland

Table of Contents

List of Figures iii

List of Appendices iv

Acknowledgments v

Abstract 1

1 Introduction 2

2 Explosive Volcanic Processes and Products 4

2.1 Magmatism at Continental Rifts *4*

2.2 Volcanic Features in Continental Rifts *5*

2.2.1 Central Volcanic Structures 5

2.2.2 Volcanic Fields 6

2.3 Controls on Magmatic Strain Accommodation *6*

3 Study Area 7

3.1 East African Rift *7*

3.2 Turkana Depression *8*

3.3 Mt Marsabit *9*

4 Analytical Methods 10

4.1 Data Collection *10*

4.1.1 Mapping 10

4.1.2 Confidence Levels 11

4.2 Clusters *11*

4.2.1 Kernel Density Clusters 11

4.2.2 Near Neighbor Distance Clusters 11

4.3 Morphology Analysis *12*

4.4 Poisson Nearest Neighbor Analysis *12*

4.5 Linear Arrays 12

4.6 Basement Structures 13

5 Results 15

5.1 Mapping 15

5.2 Morphology Analysis 15

5.2.1 High confidence elliptical features 15

5.2.2 Kernel Density Clusters 15

5.2.3 NNd Clusters 16

5.3 Poisson Nearest Neighbor Analysis 16

5.4 Linear Arrays 16

5.5 Basement Structures 17

6 Discussion 18

6.1 Distribution 18

6.2 Morphology Trends 19

6.2.1 Cluster Trends 19

6.2.2 Secondary Trends 19

6.3 Differences in Morphology and Linear Array Trends 20

6.4 Controls on Magmatic Conduits on Marsabit 21

6.4.1 Volcanic Trends and Basement Structures 22

6.4.1 Localized Stress Field Rotations 22

6.4.2 Exploitation of Riedel Shears 23

6.5 New Proposed Model: A combination of controls 24

6.5.1 Model Limitations 24

7 Conclusion 25

Works Cited 27

Figures 33

Appendices 56

List of Figures

Figure 1 The East African Rift. 33
Figure 2 Diagrams illustrating cross cuts of scoria cones and maar craters... 34
Figure 3 Photograph of fractures and a dike cross cutting sedimentary layers in Utah, USA.. 35
Figure 4 Cartoon demonstrating Anderson's theory of faulting in an extensional environment.. 36
Figure 5 A cartoon simplifying a continental rift like the EAR, fueled by a mantle plume.. 37
Figure 6 Mantle plumes are fueling the extension in the EAR 38
Figure 7 Trends of volcanic features and faults in East Turkana. 39
Figure 8 An example of a cone in the town of Marsabit.. 40
Figure 9 An example of a DTM from the Nyambeni Hills. 41
Figure 10 An example of a maar assigned a high confidence score 42
Figure 11 An example of Kernel Density Clusters.. 43
Figure 12 A cartoon demonstrating the Minimum Bounding Geometry tool in ArcGIS Pro. 44
Figure 13 MATLAB 3-point lineament identification. 45
Figure 14 Feature types and confidence level categories for mapped features.. 46
Figure 15 Distribution of maar craters, cones, and elliptical high-confidence features used for the morphology analysis. 47
Figure 16 A comparison between elevation and area of Mt Marsabit volcanic centers. 48
Figure 17 Six clusters are defined by Kernel Density... 49
Figure 18 Clusters defined by Near Neighbor distance (NNd) 50
Figure 19 Histograms of KDE, and rose diagrams of trends for possible linear arrays identified in two different width/length combinations.. 51
Figure 20 Selections from Key's map of the Mt Marsabit area (1987) 52
Figure 21 Rose Diagrams displaying trends identified in the strike of planes and trend of lines, as mapped by Key (1987) 53
Figure 22 Schematic illustrating Riedel shears developing in a strike slip environment 54
Figure 23 Riedel shear schematics with an assumed WNW-ESE direction of extension 55

List of Appendices

Appendix A: ArcPy Script 56

Appendix B: Technical Walkthroughs 56

Appendix C: All mapped volcanic centers 56

Appendix D: KMZ file of mapped volcanic centers 56

Appendix E: Georeferenced map of volcanic centers 56

Appendix F: Results of Poisson Nearest Neighbor Analysis 56

Appendix G: Rose diagrams of possible linear arrays 56

Appendix H: Results of KDE analysis on possible linear arrays 56

Acknowledgments

I would like to express my heartfelt thanks to the Geography and Sustainability Department and Geological Sciences Department at Salem State University for providing me with an exceptional academic environment in which to pursue my graduate studies. Special thanks to Dr. Sara Mana, Dr. James Muirhead, Dr. Marcos Luna, and Prof LaVerde for their guidance, support, and encouragement throughout my studies.

I am also deeply grateful to my colleagues and mentors who have played a crucial role in shaping my research and academic career. I would like to thank Kym Pappathanasi, Sharissa Thompson, Rick Allmendinger, Chris Morley, Bob Reynolds, and Sarah J Oliva for their invaluable assistance, advice, and constructive feedback.

I would like to acknowledge the generous support of the AGU, GSA, and ESIP for their grants, which have provided me with the necessary resources to conduct my research. Without their financial support, this research would not have been possible.

This work is dedicated to Matilda (my biggest obstacle and motivation) and my Dad (who loved maps).

Abstract

Previous research has demonstrated that the morphology and linear arrays of extrusive volcanic features indicate the presence and orientations of the magmatic constructs that feed them. In extensional tectonic environments, like the East African Rift (EAR), trends of these subsurface dikes can be controlled by inherited lithospheric structures or by the direction of applied stress. Mapping extrusive volcanic features with remote sensing allows for detailed geo-spatial analysis that can reveal valuable data regarding the state of stress in the region or the presence of pre-existing fractures and other lithospheric structures.

Mt Marsabit, Kenya (2.32°N, 37.97°E) is a basaltic shield volcano located on the eastern edge of the Turkana Depression in Northern Kenya. The Turkana Depression is a topographical low area of extensional deformation linking the Main Ethiopian Rift (MER) and the Kenya Rift, characterized by a very thin rifted lithosphere (50-60 km; Fishwick, 2010; Kounoudis et al., 2021). While there is typically a predominant north-south orientation of structural and volcanic features in the EAR, some features in east Turkana (e.g. the Dilo-Durkana, Mega, and Hurri Hills volcanic fields) demonstrate superficial NE-SW trends, oblique to the main rift trend. The monogenetic volcanic field situated on Mt Marsabit is no exception and hosts hundreds of tuff cones and maar craters exhibiting an apparent NE-SW trend. The cause of these trends is so far unknown.

Here we present data from the mapping and analysis of extrusive volcanic features on Mt Marsabit in an effort to improve our understanding of the tectonic and structural controls on crustal magma transport in this off-axis region of rifting. Analysis of the morphology of these features is performed in ArcGIS Pro while alignments of these features are analyzed in MATLAB. Previously published geological maps are also examined. This volcanic field exhibits a strong northeast-southwest trend in both morphology and linear arrays. Similar trends are observed in other volcanic fields in the eastern extent of the Turkana Depression. The obliquely oriented dikes in these fields may be a result of a combination of controls: en-echelon deformation zones associated with a component of strike-slip deformation; and a rotation of the local stress field.

1 Introduction

The use of remote sensing and GIS to analyze the shape (morphology) and distribution of volcanic centers has become a popular method of examining magmatic strain accommodation over the decades (Paulsen and Wilson, 2010; Le Corvec et al., 2013a; Le Corvec et al., 2013b; Muirhead et al., 2015; Mazzarini et al., 2016; Robertson et al., 2016; Franchescini et al., 2020). The morphology and distribution of volcanic centers can reveal valuable data on the state of tectonic stress and inherited crustal structures in a variety of tectonic settings (Nakamura, 1977; Isola et al., 2014; Le Corvec et al., 2013b). It has been established that trends of linear arrays and the morphology of some volcanic features can reflect the locations of the subsurface feeder dikes that feed these features (Paulsen and Wilson, 2010). Magmatic intrusions exploit weaknesses in the lithosphere or surface rocks (Rubin, 1995). In extensional environments, weaknesses and fractures that dikes exploit during their ascent can be controlled by two factors: the state of stress, and/or previously existing weakness in the lithosphere (Ebinger et al., 2005; Le Corvec et al., 2013b; Robertson et al., 2016).

Mt Marsabit is a basaltic shield volcano located in northern Kenya in the Turkana Depression, a segment of the East African Rift (EAR) (**Fig 1**). Mt Marsabit hosts a monogenetic (formed in one eruption) basaltic volcanic field containing hundreds of cones and craters. Kenyan and British field geologists had long observed these extrusive volcanic features are concentrated in NE trending swaths. The shapes of these features, particularly maar craters, have also been observed to “point” to the NE (Williams, 1970; Key 1987; Key et al., 1987; Key et al., 1989).

A variety of methods have been employed previously to map and analyze monogenetic volcanic cones and craters using different remote sensing techniques and analytical software (Paulsen and Wilson, 2010; Le Corvec et al., 2013; Muirhead et al., 2015; Muirhead et al., 2022). What can these methods tell us about the state of tectonic stress around Mt Marsabit? Can they reveal the presence of lithospheric structures?

Here we present data derived from the mapping and analysis of the morphology (shape) and distribution of the volcanic centers that make up the Mt Marsabit volcanic field. We also analyze trends mapped in a previously published reconnaissance geological map of the area in an effort to understand pre-existing basement structures. These analyses will provide valuable information about Mt Marsabit and add to a growing body of work that uses geospatial analysis to further understand the dynamics of the EAR.

2 Explosive Volcanic Processes and Products

2.1 Magmatism at Continental Rifts

A continental rift is a zone of extension defining a nascent plate boundary. In this tectonic regime, the Earth's lithosphere is stretched, causing thinning and cracking of the crust over millions of years. This deformation is often accompanied by brittle faults, ductile shear zones, and magmatic activity. Sometimes rifting can lead to the formation of new ocean basins, as the stretching of the lithosphere allows magma to rise to the surface and create new oceanic lithosphere (Vink et al., 1984). Passive and active continental rifting refer to different processes producing continental breakup or separation (Turcotte and Emerman, 1983).

Passive continental rifting occurs when the lithosphere (the rigid outer layer of the Earth) begins to stretch and thin due to internal forces, but there is no active tectonic pulling apart (Turcotte and Emerman, 1983). This type of rifting is characterized by a broad zone of faulting and sedimentation that may eventually lead to the formation of a new ocean basin. The Red Sea and the Gulf of California are examples of passive continental rifts.

Active continental rifting, on the other hand, is initiated by an upwelling of magma (also called a mantle plume) from the Earth’s mantle, which causes the lithosphere to stretch and thin (Vink et al., 1984; Ebinger, 2005). When the resulting tensional stress exceeds the strength of the lithosphere, rifting results. The resulting network of faults and fractures may lead to the formation of a new ocean basin (Vink et al., 1984). The East African Rift System is an example of an active continental rift.

After initiation, rifting can then be driven by one or more factors: lithospheric buoyancy, mantle tractions, and subduction-related forces (Brune et al., 2023).

Rising magma from the mantle causes lithospheric buoyancy (Brune et al., 2023). The lithosphere in the rifting area becomes less dense and therefore rises, forming topographic highs like the Ethiopian and Kenyan Plateaus of the EAR.

Mantle traction can be thought of as a pulling force that acts on the lithosphere, driven by the process of convection in the mantle below (Brune et al., 2023). As mantle material moves, it can drag on the base of the lithosphere. This force can cause the lithosphere to move in the same direction as the mantle material.

The subduction of the lithosphere is the last possible driving force of rifting (Brune et al., 2023). As dense oceanic plate subducts beneath a continental plate, it can pull attached continental plates down with it (“slab-pull”). Slab-pull can cause the continental plate to stretch and thin, further driving rifting.

Continental rifts are highly volcanic (Ebinger, 2005; La Femina, 2015). Volcanoes tend to be located on the rift valley margins (off-axis), and intrusive rocks are found in the rift valley itself. Magma can be generated by decompression melting as mantle rocks are moved towards the Earth’s surface (Brune et al., 2023). As mantle material rises, they experience a decrease in pressure, causing a decrease in the melting temperature of the rock. As a result, the upwelled mantle material melts, creating magma. Magma can also be generated by the elevated temperatures from the mantle plume (Brune et al., 2023).

Magma chambers are areas where the magma rising from the mantle is pooling within the crust and feeding volcanic eruptions. Faults and cracks in the lithosphere are exploited by magma, forming dikes- tabular vertical intrusive igneous features that cut across preexisting rock layers. By studying the composition, orientation, and relationships of dikes to other rock layers, scientists can gain insights into the processes that have shaped the Earth over time.

2.2 Volcanic Features in Continental Rifts

2.2.1 Central Volcanic Structures

As discussed, continental rifts tend to be highly volcanic areas (LaFemina, 2015). The type of volcano that forms depend on the composition of the magma, and the way in which it erupts.

Shield volcanos are low-profile volcanoes that form when fluid, basaltic lava flows out over a wide area. Shield volcanoes are the most common type of volcano on Earth and are found in many different parts of the world in different tectonic settings. Mt Fuji, Japan, is a famous example of a shield volcano (de Silva and Lindsay, 2015).

A composite volcano, also known as a stratovolcano, is built up over time by repeated eruptions of viscous magma and volcanic ash. These volcanoes are typically steep-sided, symmetrical cones with a concave-shaped summit crater. Composite volcanoes are some of the largest and most dangerous volcanoes in the world. While more commonly found at subduction zones, Mt Meru, Longonot, and Elgon in the EAR are all composite volcanoes (de Silva and Lindsay, 2015).

2.2.2 Volcanic Fields

A volcanic field is an area that contains numerous volcanic centers like vents, fissures, cones, or craters (de Silva and Lindsay, 2015; Valentine and Connor, 2015). These areas are characterized by a high concentration of volcanic activity over a relatively broad geographic area. While there is no strict definition, they usually consist of a cluster of tens to hundreds of small explosive volcanic centers that share a common magma source. Volcanic fields can be monogenetic (erupted only once) or polygenetic (repeated eruptions) (Valentine and Connor, 2015).

Monogenetic volcanic fields are common in areas where there is a lot of magma available, such as continental rifts. They often feature two kinds of volcanic centers: maar craters and scoria cones (Németh, 2010). A maar crater (**Fig. 2**) is a circular, flat-bottomed crater that forms during explosive interactions between magma and water (de Silva and Lindsay, 2015). Maar craters can have a diameter anywhere from a few hundred meters to greater than 2 km and are surrounded by a tuff ring, sometimes 10s of meters high, consisting of pyroclastic and fall deposits ejected during the eruption (White and Ross, 2011).

Scoria cones (also known as cinder cones) commonly erupt as high-volume lava fountains but are not as violently explosive as eruptions that form maar craters. These cones are typically less than 300 meters high and composed of accumulated lapilli and bombs with wide and often asymmetrical craters at the summit. The slopes of fresh cones are not steep, averaging 30°, but may become steeper after erosion (Valentine and Connor, 2015) (**Fig. 2**).

2.3 Controls on Magmatic Strain Accommodation

Magmatic strain accommodation is a way of describing how the crust accommodates the growth and direction of magmatic conduits and dikes. Volcanic centers in volcanic fields are fueled by feeder dikes, which are tabular conduits that transport magma from magma chambers to the surface during volcanic eruptions (Gonnermann and Taisne, 2015). Most feeder dikes, especially from relatively young volcanoes, cannot be seen from the surface and range in size from 1 to 10 meters wide and up to 100 km long (Blatt and Tracey, 1996). Two factors control the propagation of dikes: pre-existing weaknesses in the surrounding rock, and local tectonic stress (Le Corvec et al., 2013a and 2013b).

Dikes exploit weaknesses in rock (**Fig. 3**). They can also form in relation to the direction of regional tectonic stress (**Fig 4**). Anderson's Theory of Faulting (**Fig. 4A**) states that the orientations of faults and fractures are controlled by the three principal stresses: the greatest (σ_1), intermediate (σ_2), and least (σ_3)

compressive stress (Anderson, 1905). In an extensional environment, σ_1 is vertical and σ_2 and σ_3 are horizontal (**Fig. 4B**). Jointing and faulting can occur when there is a great enough difference between σ_1 and σ_3 (**Fig 5**). Dikes can exploit those fractures, which would propagate perpendicular to σ_3.

3 Study Area

3.1 East African Rift

The East African Rift (EAR) is an active continental rift consisting of a 3,000 km long complex system of diachronous rifts that extends from the Middle East to the Mozambique channel, passing through several East African countries (**Fig. 1A**) (Chorowicz, 2005; Ebinger, 2005; Corti, 2009; Ring, 2014; Macgregor, 2015). Here, the African Plate is splitting into two plates: the Nubian Plate to the west and the Somali Plate to the east. The EAR is traditionally split into two main branches: the Eastern branch and the Western branch. Each branch consists of a number of kinematically linked rifts.

The Eastern branch is the northernmost branch of the EAR, extending from Ethiopia to Malawi (**Fig. 1A**). This branch is characterized by high volcanic activity and a narrow rift valley, with steep walls that rise to over a kilometer above the valley floor (Ebinger, 2005). Topography is characterized by steep-sided escarpments, fault-block mountains, and volcanic peaks (Ring, 2014). The Eastern branch is highly volcanic, with numerous active and dormant volcanoes along its length.

The Western branch is the southernmost and shortest branch, extending for approximately 500 km from Lake Malawi to the Luangwa Valley in Zambia (**Fig. 1A**) (Chorowicz, 2005; Ring, 2014; Macgregor, 2015). This branch is characterized by a broad and shallow rift valley, with relatively low volcanic activity and few large deep lakes. The Western branch is considered more stable than the Eastern branch, with relatively low seismic activity and slow rates of tectonic movement (Chorowicz, 2005; Ring, 2014). The topography of the Western branch is characterized by a broad, shallow valley floor and relatively low-lying mountain ranges on either side. It is relatively less volcanic, with the exception of the Virunga Mountains in Uganda, Rwanda, and the Democratic Republic of Congo.

The Eastern and Western branches are separated by the Tanzania Craton, a block of old and stable continental crust that dates back over 2.5 billion years (Ritsema et al., 1998). The craton is surrounded by younger, less stable rocks that have been affected by tectonic activity, including the rifting of the East African region.

Computational modeling suggests that extension at the EAR is a product of lithospheric buoyancy (Rajaonarison et al., 2021). Seismic studies also suggest the presence of a low-velocity zone under the lithosphere (Sippel et al., 2017). At the EAR, the lithosphere is undergoing extension due to one or more asthenospheric upwellings in the upper mantle, often referred to as mantle plumes (Nelson et al., 2012). As the mantle plume rises, it facilitates the melting of the lithosphere and it exerts an upward force on the overlying lithosphere, which causes the lithosphere to stretch and thin (**Fig. 6**). This plume activity is believed to be responsible for the extensive volcanic activity observed in the region (Wood and Guth, 2019).

3.2 Turkana Depression

The Turkana Depression is a volcanically and seismically active topographic low situated between the uplifted Ethiopian Plateau and Tanzanian Craton, consisting of north-south oriented half-graben basins bounded by north-south striking rift bounding faults (**Fig. 1A**) (Bosworth and Strecker, 1997; Morley et al., 1992). Where the narrow rift valleys to the north and south rarely exceed 100 km in width, the Turkana Depression exceeds 300 km (Ebinger et al., 2000). Geophysics has revealed a very thin lithosphere, sometimes less than 25 km (Sippel et al., 2017). While rifting in the Turkana Depression is thought to have initiated approximately 25 million years ago, the anomalous width, lack of topographic highs, and thin lithosphere are thought to be controlled by preexisting lithospheric structures formed by rifting in the Mesozoic (Brune et al., 2017).

Episodic GPS measurements, earthquake slip vector directions, and geologic indicators suggest that the modern extension in the Turkana Depression occurs in a roughly E-W direction at a rate of a few millimeters a year (Saria et al., 2014; Stamps et al., 2014). Modeling suggests extension has held steady for the past 10 to 12 million years (Iaffaldano et al., 2014; DeMets and Merkouriev, 2016). N-S trends are seen in the center of the Turkana Depression, closest to the rift axis. For example, the trends of high confidence elliptical volcanic features on the South Island volcano in Lake Turkana trend 007°, and fault and fracture systems just south of Lake Turkana on the Barrier Island trend 012° (**Fig. 7;** Muirhead et al., 2022). Additionally, rift normal faults in the area trend 003° (Macgregor, 2015; Mazzarini et al., 2022).

Conversely, two large fault zones found on either side of the lake, the Buluk and Kataboi Fault Zones, trend 050° (**Fig. 7**; Vétel and Le Gall, 2006). East of Lake Turkana, four volcanic fields display trends ranging from 015 to 047°, including the Mt Marsabit, Hurri Hills, Dilo-Durkana, and Mega volcanic fields (Franceschini et al., 2020; Mazzarini et al., 2022). These volcanic fields have much in common with Mt

Marsabit: they all formed in the Quaternary and are off-axis, distributed along a broad 500 km-long N-S array from the southern extent of the Main Ethiopian Rift to the Kenya Rift. The locations and similarities in trends may suggest that the same controls on the development of magmatic conduits operate in each volcanic field.

3.3 Mt Marsabit

Mt Marsabit (Kenya) is an off-axis volcano situated in the Turkana Depression, approximately 130 km east of the southern tip of Lake Turkana (**Fig. 1B**). Magmatic activity began in the late Miocene (Kaeser et al., 2007). Most of the construction of Mt Marsabit occurred in the Pliocene from Hawaiian-type volcanism- effusive eruptions of low viscosity, basaltic lava- which formed a shallow dipping shield (Key, 1987; Key et al., 1987). Volcanic activity continued during the upper Pliocene to the Quaternary resulting in the formation of a monogenetic volcanic field containing hundreds of maar craters, tuff cones, and scoria cones from comparatively more violent eruptive style volcanism compared to the earlier lava flow phases (Key, 1987; Key et al., 1987).

It has been long observed that the extrusive volcanic features on the slopes of Mt Marsabit are concentrated along northeast trending belts (Williams, 1970; Key 1987; Key et al., 1987). Considering the east-west modern documented extension and the north-south trending border faults of the Turkana Depression, the controlling factors of the northeast trends on Mt Marsabit are unknown.

4 Analytical Methods

4.1 Data Collection

4.1.1 Mapping

An area of approximately 9,000 km^2 was mapped using Google Earth Pro (v7.3.4) and techniques adapted from Paulsen and Wilson (2010), Le Corvec et al. (2013b), and Muirhead et al. (2015). Image resolution in Google Earth Pro ranges from 15 meters to 15 centimeters and is ample for identifying and mapping volcanic features. Previous work comparing elevation data from the U.S. Geological Survey National Elevation Dataset and Google Earth Pro found that Google Earth Pro is accurate within 2.27 meters (Wang et al., 2017). Additionally, files produced in Google Earth Pro are compatible with GIS software, such as ArcGIS Pro, enabling data analyses.

The volcanic field on Mt Marsabit was informally separated into five sections and systematically examined for extrusive volcanic features. Features were classified, numbered, and noted in an Excel spreadsheet with UTM coordinates and elevation. Each identified volcanic object is analyzed using oblique views to identify the morphometric extent. Idealized extents of scoria and tuff cones are drawn using the polygon tool in conjunction with elevation profiles. A minimum of four elevation profiles are taken across the figure to identify the spatial extent of the feature (**Fig. 8**). Due to erosion, cone rims are often incomplete, and these are mapped using best fit ellipses. The outer rim of each maar crater is drawn with the polygon tool after the area has been examined using oblique views and elevation profiles.

After initial mapping in Google Earth Pro, each feature is compared to a digital terrain model (DTM) created by Esri using data from Airbus, USGS, NGA, NASA, CGIAR, NLS, OS, NMA, Geodatastyrelsen, GSA, and GSI. The DTM indicates rates of inclined terrain, which is a helpful tool to ensure accurately drawn polygons (**Fig.9**), especially where visibility is limited due to vegetation, agriculture, or buildings (particularly in the town of Marsabit, located north of the summit).

Mapping, by nature, is a subjective process. To ensure objectivity, each informal section is examined individually by collaborators and reviewed three times, at a minimum. Areas populated with many volcanic features were reviewed 10 or more times.

4.1.2 Confidence Levels

Feature polygons are assigned a confidence level using methods adapted from Paulsen and Wilson (2010) (**Fig.10**).

- A high confidence level (CL1) indicates that the feature has undergone minimal erosion and displays prominent elevation relief. The polygon of a CL1 feature accurately represents the extent of that feature.
- A mid confidence level (CL2) feature may have undergone some erosion, but the best fit ellipse is still an accurate representation of the extent of the feature.
- A low confidence level (CL3) indicates a highly eroded feature with little elevation relief. The level of erosion and lack of relief makes it difficult to determine the true extent of the feature, and the resulting polygon may not be an accurate representation.

Paulsen and Wilson (2010) state that minimally eroded, elliptical features are the best indicators of the magmatic intrusions that feed them. To this end, volcanic centers with a CL of 1 or 2 and a long/short axis ratio of 1.2 or greater are selected for the morphology analysis. As the polygons of CL3 features may not be an accurate representation of feature extent, they are not utilized in the morphology analysis. The central points of CL3 features are used in linear array analyses.

4.2 Clusters

We use two methods to identify clusters of features on Mt Marsabit: Kernel Density (Section 4.2.1) and Near Neighbor distance (Section 4.2.2). Both techniques use elevation and the geographic centers of extrusive volcanic features as calculated in ArcGIS Pro (v.3.0.2) to identify clusters. Each resulting cluster will be analyzed to find trends in the morphology of features within them.

4.2.1 Kernel Density Clusters

Kernel Density is defined using the *Kernel Density* tool in ArcGIS Pro, which calculates magnitude-per-unit area from a population of distributed objects (**Fig. 11**). A Kernel is a weighting function that is fitted over each object. Objects that are close together overlap and form a stronger Kernel, which indicates density.

4.2.2 Near Neighbor Distance Clusters

Clusters are also defined by Near Neighbor distance (NNd) using hierarchical clustering tools in MATLAB R2020b (v.9.9.0.1). Clusters are classified by the distance between points- in this case, the geographic centers of volcanic features. Different NNd thresholds are used to define clusters- in each cluster, the maximum distance between points must be less than the NNd threshold. We use two NNd thresholds, resulting in two sets of clusters: 11,000-meter and 8,000-meter.

4.3 Morphology Analysis

The angle of elongated volcanic features like vents, cones, and craters reflects subsurface dike trends (**Fig. 4**) (Breed, 1964). The best indicating features are elliptical and minimally eroded, allowing for an accurately drawn polygon (Paulsen and Wilson, 2010). To this end, we selected volcanic centers with a CL of 1 or 2 and a long/short axis ratio of 1.2 or greater for the morphology analysis. As the polygons of CL3 features may not be an accurate representation of feature extent, they are disregarded.

The ArcGIS Pro data management tool Minimum Bounding Geometry is used to find the orientation of the long axis of volcanic features (**Fig. 12**). This tool fits rectangular bounding boxes over shapefiles representing the features- the long axis of the resulting rectangle is the trend of the feature. Other GIS programs, like QGIS, have similar tools.

ArcPy code used for the morphology analysis is reported in **Appendix A.** Walkthroughs detailing the manual process are detailed in **Appendix B.** Rose Diagrams are created using Stereonet 11 (Allmendinger et al., 2013; Cardozo et al., 2013).

4.4 Poisson Nearest Neighbor Analysis

The Poisson Nearest Neighbor (PNN) analysis is a method of assessing if a group of points is random, regulated, or clustered. It accomplishes this by comparing the mean Near Neighbor distances (NNd) of a population to an idealized statistical model (Clark and Evans, 1954). The results allow us to determine if the distribution of volcanic centers on Mt Marsabit is clustered or random.

The MATLAB image processing package GIAS (Beggan and Hamilton, 2010) is used to perform the PNN. After inputting the UTM coordinates of volcanic centers (calculated in ArcGIS), GIAS determines the minimum, mean, and maximum NNd, the R and c statistical values, and the density of the volcanic field. The density of the volcanic field is used to calculate the maximal length of linear arrays (Le Corvec et al., 2013b).

4.5 Linear Arrays

While it has been long established that linear arrays of monogenetic volcanic features indicate subsurface dikes, a systematic, quantifiable, and repeatable method has been more difficult to define (i.e. Nakamura, 1977; Paulsen and Wilson, 2010) and published datasets are acquired with a varying range of rigor, and some tend to be subjective and not repeatable.

We define a linear array as three volcanic features that fall within predetermined width and length tolerances (**Fig. 13**). To identify linear arrays in a quantifiable manner, we utilize a MATLAB script by Le Corvec et al. (2013b) to calculate regression lines between the central points of mapped volcanic features. A variety of different width and length tolerances are utilized, resulting in many sets of possible linear arrays. Trends that repeat in the majority of the width-length combinations can be considered reliable indicators of linear arrays, and therefore indicators of subsurface feeder dikes (Le Corvec et al., 2013b).

The number of possible linear arrays identified by the script escalates as width and length tolerances increase. Many of these suggested arrays are digital artifacts and not geologically substantial. To filter artifacts, the Distribution Fitter application in MATLAB is used to establish kernel density estimates (KDE) for the results of the three-point alignment script. KDE is a non-parametric method used to estimate the probability density function of a given dataset. It is often used in statistical analysis and data visualization to understand the underlying distribution of data. KDE can be visualized as a continuous curve that approximates the probability density function of the dataset. The curve can be used to identify areas of high or low density within the data.

The KDE analysis can artificially misconstrue results around 000 and 180°. Compass azimuths are circular- a linear array that trends at 000° could also be considered to trend at 180°; an array that trends at 090° could also be considered to trend at 270° and so on. Conventionally, angles are given from 000-180°. The KDE reads results like a number line, with a definite beginning and end. Thus, it does not link and properly evaluate angles close to 000 or 180°. To work around this, a few length/width combinations have also been analyzed through an extended range. To do so, trends resulting from the 3-point alignment code are increased and decreased by 360° increments and added to the KDE. This extends the range to -360 to 540°. After running MATLAB for this extended interval, we then consider the trends identified from 000-180° to identify predominant peaks.

Walkthroughs detailing the 3-point code and KDE analysis in MATLAB are detailed in **Appendix B.**

4.6 Basement Structures

As discussed, preexisting lithospheric structures can control trends in dike propagation since magma exploits fractures and planes of weaknesses in the lithosphere. These structures are found in basement rock- the oldest and most fundamental layer of rock that underlies the surface of the Earth. It typically consists of igneous and metamorphic rocks, which are formed through volcanic or tectonic activity and are generally crystalline and non-fossiliferous.

Basement rock is generally buried under layers of sedimentary rock and soil and can be found at varying depths depending on the location. In some places, it may be exposed at the surface due to erosion or tectonic activity. Basement rock is not visible in the Marsabit volcanic field as it is located on a shield volcano consisting of extensive quaternary basalts. In the 1987 reconnaissance geologic map by Key, two outcrops of pre-rift basement rocks are visible in the vicinity of Mt Marsabit: the Precambrian Korr Complex and the Kotim Gneiss (Key, 1987; Key et al., 1987). The strike of planar fabrics is mapped in both outcrops.

The strike of a planar fabric is a geological term that refers to the orientation or direction of a horizontal line that lies in the plane of a geological feature such as a rock layer, fault, or fold. It can be visualized as the intersection of the planar feature with the horizontal surface. The strike is the orientation of this line from the North and is typically reported as an azimuth from 000° to 360°.

The trends of linear fabric, such as lineations in metamorphic rocks, were also mapped. Lineations in gneiss are typically formed by the alignment of elongated mineral grains or other structural features in the rock (Hobbs et al., 2011). The trend of lineations refers to the overall direction or orientation of these elongated features in the rock. These trends can provide insights into the deformation history of the rock, such as the direction and intensity of the forces that caused the elongation and alignment of the mineral grains (Etheridge, 1983; Hobbs et al., 2011). For example, if lineations in gneiss are oriented in a consistent direction, this could suggest that the rock was subjected to strong compressional forces in a particular direction. If lineations are oriented in multiple directions, this may suggest that the rock has undergone no deformation in a preferential orientation or has been affected by complex deformation possibly involving multiple tectonic events.

Key’s geologic map was uploaded and georeferenced in Google Earth Pro (v7.3.4). Strikes of planes and trends of lines are traced in Google Earth Pro. Similar to the Morphology analysis (section 4.3), the resulting KMZ file is uploaded to ArcGIS Pro, where the angle of each line is calculated. The resulting trends were then examined in Microsoft Excel. Rose diagrams of the trends were created using Stereonet 11 (Allmendinger et al., 2013; Cardozo et al., 2013).

5 Results

5.1 Mapping

A total of 613 volcanic centers were mapped on the slopes of Mt Marsabit using the WGS 84 / UTM 37N coordinate system. The entirety of the mapping process took approximately 18 months. The convex hull encompassing all volcanic centers measured has an area of 7.3 million km^2 and trends 047°. Of the 613 features, 62 (10%) are maar craters and 551 (90%) are tuff or scoria cones (**Figs. 14 and 15**). **Appendix C** contains the complete dataset of mapped features. The KMZ file is contained in **Appendix D** and a georeferenced map is available in **Appendix E.**

Elevation ranges from 416 to 1654 meters above sea level (msl) (**Fig. 16A**). The area of volcanic centers on Mt Marsabit range extensively from 3056 m^2 to 5540 km^2 (**Fig. 16B and C**). Generally speaking, scoria cones tend to have a smaller area than maar craters. Less than 10% of cones are greater than 800,000 m^2, while 40% of maar craters are greater than 800,000 m^2. Almost 80% of all features are less than 480,000 m^2. There does not appear to be a relationship between elevation and area (**Fig. 16D**).

Approximately 30% of all features meet morphology criteria analysis- 27% of all Maar craters (16 features) and 30% of all cones (169 features) (**Fig. 15).** These features appear to be evenly distributed on Mt Marsabit. Most (80%) of the features that meet morphology criteria have an area less than 0.5 km^2, and 70% are situated between 500 and 1000 msl.

5.2 Morphology Analysis

5.2.1 High confidence elliptical features

Cones and craters with a long/short axis ratio greater than 1.2 and a confidence level of 1 or 2 are candidates for morphology analysis. Rose diagrams of the orientations of the long axes of these elliptical, high confidence volcanic centers indicate a strong NE trend. There also appear to be secondary trends to the NNE and ENE in the rose diagram (**Fig. 15B**).

5.2.2 Kernel Density Clusters

Six clusters are identified by Kernel Density (**Fig. 17).** Because only areas with a density greater than 0.16 centers per kilometer are considered a cluster, not all features fall within cluster boundaries. Rose diagrams are created from the long-axis trends of features within each cluster that meet morphology analysis criteria.

Three modes are observed: N-S, NE-SW, and E-W (**Fig. 17**). The NE-SW is the dominant peak, found in KD1,2,3,4,5. The N-S orientation is seen in KD1,2,6, and the E-W is found in KD,1,2,4,6. KD4 only contains three analyzed features, each displaying a different trend. KD2, which straddles the summit of Mt Marsabit, has the greatest number of features and the greatest density of 0.48-0.57 centers per meter.

5.2.3 NNd Clusters

Near Neighbor distance (NNd) analyses with thresholds of 11,000-meter and 8,000-meter are used (**Fig. 18**). With this technique, all features are considered part of a cluster. Only features that meet morphology analysis criteria are considered here.

Five clusters are defined using an 11,000-meter threshold, each cluster containing 21 to 52 high-confidence, elliptical features. Four of the five clusters display a strong NE trend. Three clusters are bimodal, displaying NE and E-W trends. Interestingly, Cluster 11000.D, situated over the summit, has a primary E-W trend.

Ten clusters are defined using an 8,000-meter threshold. One cluster, 8000.F, contains no features that meet morphology analysis criteria. The other clusters contain between 10 and 37 high-confidence, elliptical features. Seven clusters display a strong NE trend and two are bimodal with trends to the NE and E-W. Cluster 8000.A could be considered trimodal, with evenly pronounced trends to the NE, E-W, and N-S.

5.3 Poisson Nearest Neighbor Analysis

The density of volcanic centers on Mt Marsabit is calculated to be $8.24E^{-08}$ per square meter. The minimum nearest neighbor distance is 71 meters, and the max is 12,618.22 meters, with the average being 1,091.3 meters. As R and c are outside the $\pm 2\sigma$ of the expected levels, the volcanic features in Mt Marsabit display a clustered distribution. The distance maximal for the generation of lineaments is 4,363 m. Detailed results are provided in **Appendix F.**

5.4 Linear Arrays

Five width tolerances are used to define linear arrays: 10, 20, 30, 40, and 50 meters. Length tolerances are used in intervals of 500 meters, from 3360-5360, with 4360 (the distance maximal identified in the PNN analysis) as the median length tolerance used. This results in 25 different combinations of width and length tolerances used to identify possible linear arrays (**Appendix G**). The results of the KDE analyses are detailed in **Appendix H.**

After the KDE, one trend is present in all 25 width and length tolerances: 043°, with frequency ranging from 0.054 to 0.017. A secondary trend of 160° is visible in 18 of the 25 combinations but is smaller by an order of magnitude- frequency ranges from 0.004 to 0.002.

Fig. 19 reports rose diagrams and KDE for two width/length combinations. Panel A displays results for 252 possible linear arrays with a 10 meters width tolerance and 3360 meters length tolerance. The primary trend of 043° is prominent in both KDE and the rose diagram. Panel B displays results for 1,160 possible arrays identified using larger thresholds: 50 m-wide and 3860 m-long. While not as dense as the first combination, the primary 043° trend is still prominent. The smaller, secondary peaks present in other length and width tolerance combinations are less visible. Overall, the density is much lower, but the proportions of the primary and secondary trends still hold true.

This KDE analysis was run again with an extended -360° to 540° range for arrays identified within a 10 meters width and 3360 meters length tolerance (**Fig 19C**). This data analysis does a better job of constraining the data distribution around the 000° and 180° by not truncating the dataset in an artificial way. Doing so we notice that the smaller 160° trend disappears. The resulting primary trend peaks at 048°, which is consistent and within five degrees of the primary trend in the un-extended range KDE.

5.5 Basement Structures

Two outcrops of basement rock are visible in the vicinity of Mt Marsabit, as mapped by Key in 1987: the Korr Complex and Kotim Gneiss, both dated to the Precambrian (**Fig. 20**). The strikes of planes and trends of lines were examined in the georeferenced map, and rose diagrams were created from the resulting trends (**Fig. 21**).

The strike of 14 planes and 26 linear trends were mapped from the fabric of the Korr Complex. Three trends are visible in the resulting rose diagrams: NW, NNE, and NE. The strike of 25 planes and 38 linear trends were mapped from the fabric of older Kotim Gneiss, which displays a single N-S trend.

6 Discussion

Examination of the morphology and distribution of volcanic centers on Mt Marsabit reveals controlling factors in their formation. Maar craters are centralized at lower elevations than cones. Similar primary trends are revealed in the shapes and distributions of volcanic centers; however, several secondary populations are visible within morphology trends but not in linear arrays. While some of these trends are reflected in basement structures, these do not appear to be a controlling force in dike propagation on Mt Marsabit.

6.1 Distribution

It appears that most of the features are concentrated in a densely populated NE trending belt that straddles the summit of Mt Marsabit. This is confirmed by Kernel Density clusters (**Fig. 17**), where nearly half (289 features, or 47%) are concentrated in Cluster KD.2, which crosses the summit. Cluster KD.2 also displays the greatest density of features, up to 0.48-0.57 features per square km.

While cones are evenly distributed across both NNd and Kernel Density clusters, Maar craters appear more confined. No Maar craters are found in clusters KD.5 and KD.6, in the southwest portion of the mountain (**Fig. 17**). They also appear to be constrained by elevation- 97% have an elevation below 1,100 msl, where cones are more evenly distributed (**Fig 16**).

Maar Craters are formed by the explosive interactions between groundwater and magma (de Silva and Lindsay, 2015). In the 1980s, oil companies prospecting on Mt Marsabit drilled a series of boreholes around the mountain (Key 1987; Key et al., 1987). Six were drilled on the summit, and three yielded groundwater between 47 and 72.5 meters below the surface. One is still in use today: Balesa Bongole, a well on the south slope of Mt Marsabit, with an elevation of approximately 1,140 msl (Key et al., 1987). The locations of the other three boreholes are undisclosed, only described as being on or near the summit. As Balesa Bongole has an elevation of 1,140 msl and water was struck by boreholes between 47-72.5 meters below the surface, it is reasonable to believe that groundwater within Mt Marsabit would be found at an elevation around 1,067 to 1,093 meters- as mentioned earlier, all but four maars are found below 1,100 meters.

Groundwater in Mt Marsabit is thought to be confined within a lens of friable (unconsolidated, easily crumbled) matter made up of soil, pyroclastic materials, and weathered lava (Key 1987; Key et al., 1987) and is recharged by rainwater. The climate is highly seasonable, with great differences between the dry and wet seasons. These conditions constrain maar craters to lower elevations.

6.2 Morphology Trends

Trends in morphology were examined in three ways: as a whole (**Fig. 15**) and by two clustering techniques: Kernel Density and NNd. Only high confidence (CL of 1 or 2, **Fig. 10**) and elliptical (long/short ratio greater than 1.2, **Fig. 12**) volcanic centers are candidates for the morphology analysis.

6.2.1 Primary Cluster Trend

NNd clusters include every volcanic center in a cluster (**Fig. 18**). The resulting rose diagrams are multimodal: while NE is still prominent, some clusters presented 3 or 4 populations, often of the same magnitude. Including every feature in a cluster results in awkward cluster boundaries. Clusters created with an 11,000-meter threshold don't seem to make geologic sense- clusters 11000.C and 11000.D contain some very isolated features that don't look like they belong with other features in their clusters. In the 8,000-meter threshold NNd clusters, four clusters encompass the summit. This results in many features only being a few meters away from features in a neighboring cluster.

Kernel Density does not assign every volcanic center a cluster: isolated features in an area with less than 0.16 features per kilometer are not included in clusters. Still, 137 (or 74%) of all high confidence, elliptical features fall within a Kernel Density Cluster. This analysis results in more organic looking cluster boundaries that appear to follow the superficial belts of features observed by field geologists and by satellite. It is our conclusion that the trends in the long axes of features are more indicative of dike trends than isolated features.

Therefore, we consider the Kernel Density clusters to be the best method for identifying geographic trends in the long axis of high confidence elliptical features (**Fig 17**). Three clusters- KD.2, KD.3, and KD.5- display a primary NE trend. KD.4 is the most heavily populated cluster, with 81 features that meet morphology analysis criteria.

6.2.2 Secondary Cluster Trends

As discussed earlier, NE-SW is the primary trend observed in both clusters and when all features are considered together. Two secondary populations are also observed: N-S and E-W.

When examined geographically by establishing Kernel Density clusters, it appears that these secondary trends are constrained by location. N-S trending clusters are observed on the summit (KD.2), immediately west of the summit (KD.1), and the extreme southwest of Mt Marsabit (KD.6)- the site of the Korr Complex outcrop, as mapped by Key et al. (1987). E-W trending clusters are also observed on the summit and immediately west (KD.2 and KD.1). All clusters display a strong NE-SW trend, with the exception of KD.4, which hosts only three features, and KD.6, which hosts 11 features at the site of the Korr Complex outcrop. KD.1, host to 23 high confidence elliptical features, is trimodal: N-S, E-W, and NE-SW trends are observed.

6.3 Differences in Morphology and Linear Array Trends

Two analyses were performed to identify trends on Mt Marsabit: the long axes of high confidence, elliptical features (morphology), and the distribution of those features (linear arrays).

While three trends (primary XX, and secondary XX and XX) are apparent in the rose diagrams of morphology trends, only one trend is observed in the trends of linear arrays (NE). This raises an interesting question: why is only one trend visible in linear arrays, and multiple modes visible in the shapes of volcanic centers?

As discussed earlier, polygons are manually drawn around the extent of cones and maar craters. A consistent human error in drawing these polygons that would bias these data introducing an additional population of features is possible, but not likely. With the exceptions of features within the town of Marsabit and the heavily forested region of the summit, exposure is good and the extent of CL1 and CL2 features are easy to identify. For volcanic centers within the town or under vegetation, the extensive use of elevation paths and DEM files ensures the proper placement of polygons. While the use of automated processes to eliminate manual mapping can be tempting, they could introduce a whole new host of errors. The use of machine learning has not been successful in identifying the extent of features- one study only had a 40% success rate (Van Hazinga et al., 2021). It could also prove difficult to “teach” a machine to understand erosion and when to use best fit lines for a heavily eroded cone.

Wind could also explain multiple trends in the shapes of cones and craters. Mt Marsabit sustains constant winds between 22 and 28 kph for most of the year, blowing from the southeast to the northwest (Weatherspark, 2019; Windfinder, 2023). While this wouldn’t influence the orientation of the elongation of maar craters, it could affect the morphology of the scoria cones. Scoria cones are formed by the accumulation of volcanic materials that are ejected from a volcanic vent during an eruption. During an eruption, the direction and speed of the wind can influence the way these materials are deposited around the vent and can thus affect the shape of the resulting scoria cone.

Additionally, the mapping area used for the Mt Marsabit volcanic field could encompass features that are regionally isolated and which controlling factors could be distinct. For example, NNd cluster 8000.H (containing 24 features) and Kernel Density cluster KD.6 (containing 11 clusters) are located over a Korr Complex outcrop, as mapped by Key et al. (1987). 8000.H displays strong NNE-SSW and E-W trends, and KD.6 displays primary N-S and secondary E-W trends. It is possible that the dikes that fed volcanic centers in this location exploited basement weaknesses not present in the rest of the Mt Marsabit volcanic field.

Another possible cause of this discrepancy could be the result of the way the data are handled. In particular, a KDE analysis is used to weed out artifacts in lineaments produced by the three-point alignment code, while elongated cones are considered individually and not screened based on their density. As discussed earlier, 185 features met the criteria for the morphology analysis (elliptical and high confidence). A total of 23,946 possible linear arrays were identified in 25 different length and width combinations. Within this huge amount of data are digital artifacts, also known as anomalies or noise-false linear arrays. The KDE analysis is necessary to sift through this huge amount of data and identify true trends.

Finally, the presence of inconsistencies in morphology and linear array trends might highlight limitations of remote sensing. Field work and geological mapping could reveal surficial reasons, not visible in satellite imagery, for the multiple secondary populations in morphology trends.

6.4 Controls on Magmatic Conduits on Marsabit

The stress state from plate-scale tectonics often controls the formation and orientation of fractures and magmatic constructs over time, where dikes and faults form parallel to maximum compressional stress (σ_1) and perpendicular to minimum compressive stress (σ_3) in a purely extensional tectonic environment.

Trends displayed in the Mt Marsabit volcanic field cannot be explained by purely E-W extension, characteristic of the EAR. Other off-axis volcanic fields like Hurri Hills, Dilo-Durkana, and Mega display similar trends (**Fig. 7**; Franchescini et al., 2020; Mazzarini et al., 2022). If the extension was the only controlling factor, volcanic lineaments at these localities would all be expected to trend primary N-S.

Here we present models that could explain the trends found in the Marsabit volcanic field: the exploitation of Riedel shear zones and changes in tectonic stress due to localized stress field rotation.

6.4.1 Volcanic Trends and Basement Structures

Firstly, the trends of basement structures need to be considered. As mentioned earlier, pre-existing weaknesses or fractures in the shallow lithosphere can be important as magma exploits the weaknesses within the lithosphere or country rock and would follow their trends. In total, 40 structural features, including visible mapped linear and planar fabrics, were analyzed in the older Korr Complex (**Fig. 21**). These display three trends: NW (~330-350°), NNE (~030°), and NE (~050-070°). A total of 63 structural features were analyzed in the older Kotim Gneiss (**Fig. 21**) displaying one trend: N-S (~340-360°).

As mentioned earlier, two density clusters are located in an outcrop of Korr Complex rock: 8000.H and KD.6. The NNE trend displayed in 8000.H matches closely to the NNE trend in the rose diagram of strike trends for the Korr Complex (**Fig. 21**). However, there are no trends in the Korr Complex that could explain the other, equally strong E-W trend.

Additionally, structural analyses of basement features mapped by Keys et al. (1987) indicate N-S oriented lithospheric structures are predominant. Secondary N-S trends found in volcanic centers on the summit, immediately west of the summit, and the extreme southwest of Mt Marsabit (**Fig. 17**) could be exploiting these weaknesses in the basement rock. However, the N-S inherited fabric cannot be considered a controlling factor of the primary NE trend observed in the morphological analyses and linear arrays. None of the orientations found within this basement fabric analysis matches with the main orientation of the Mt Marsabit volcanic field (043°), suggesting that lithospheric fabric is not the major control of the orientations of the dike-feeder system below Mt Marsabit.

6.4.1 Localized Stress Field Rotations

Extension in the EAR is often simplified to occur in an E-W direction. While this is true for many large portions of the EAR (Saria et al., 2014; Stamps et al., 2014), episodic GPS measurements, continuous measurements, and earthquake slip vector directions indicate that microplates and large lithospheric blocks are rotated relative to the main rift (Fernandes et al., 2004; Koehn et al., 2008; Oliva et al., 2022). While an E-W extension cannot be a main factor in dike propagation on Mt Marsabit, an WWN-EES direction of extension could.

Other researchers have proposed localized stress field rotations in other parts of the EAR. A team examined local stress in relation to dike propagation in the highly volcanic Magadi-Natron-Manyara basin, located approximately 550km south of Mt Marsabit in the Eastern Branch of the EAR (Oliva et al., 2022). This study utilized data from previously published seismicity and tomography studies to create numerical and analytical models, which suggest that the extension in that region is rotated from E-W to NW-SE, a similar process as presented here.

Another example can be found in the Rwenzori horst of the Rwenzori rift in the western branch of the EAR (Koehn et al., 2008). In this study, researchers created a two-dimensional visco-elasto-plastic spring model indicating the rotation of micro-plates around the Rwenzori horst, resulting in a left-lateral strike-slip extensional regime.

6.4.2 The Exploitation of Riedel Shears

Riedel shear structures are non-parallel faults or fractures that intersect at specific angles (**Fig. 22**). In models, ideal Riedel shears form in relation to the direction of maximum compression, or σ_1. A primary set of fractures called R shears form 30° clockwise from σ_1. These are represented by the purple line in **Fig. 22.** A secondary set of fractures, called R' and represented by the green line in **Fig. 22**, form 30° counterclockwise from σ_1. These angles occur in textbook perfect models- sometimes in the field, other factors can affect angles slightly.

At large scales, Riedel shears form en-echelon deformation zones in sedimentary environments associated with strike-slip fault systems. The relationships between Riedel shears and the involved stresses have been studied in controlled environments characterized by isotropic rock formations (uniform physical properties and mineral composition) and limited to coaxial deformation regimes at or near the Earth's surface, overlying a planar basement wrench-fault system (i.e. Tanner, 1962; Wilcox et al., 1973; Moore, 1979; Ahlgren, 2001).

Evidence of Riedel shears has been found elsewhere in the East African Rift. In the Malawi rift in the Western branch of the EAR, Riedel like structures are observed in the basement rock using field observations, seismic data, and gravity data (Ring, 1994). This area, on the border of Tanzania and Malawi, displays a complicated pattern of deformation that includes numerous brittle faults that reflect R and R' angles in exposed basement rocks. There is also evidence that pre-rift border faults were reactivated in the Cenozoic as strike-slip faults.

Although surficial expressions of faults and fractures are common along the Turkana Basin, these are not visible on Mt Marsabit since they are likely overlain by the products of the intense Hawaiian-type volcanism that formed the shield in the Miocene. The Precambrian basement structures considered in **Fig. 21** do not represent faults or fractures, but the trend of the planes and lineations in metamorphic rocks. The trends of high confidence, elliptical features, and orientations of linear arrays are better used to infer the direction of fractures on Mt Marsabit, as the magmatic constructs that feed these centers would have exploited them.

If NE trending Riedel shears are a controlling factor in dike propagation on Mt Marsabit, then there must be a left-lateral sense of slip. As the motion is not purely extensional, the movement of lithospheric blocks in this locality must be oblique.

6.5 New Proposed Model: A combination of controls

A combination of localized stress field rotation and the exploitation of Riedel shears could be responsible for trends found on Mt Marsabit (**Fig. 23**). An ENE-WSW direction of oblique extension in a left-lateral strike slip environment could result in large scale Riedel shear structures. When a Riedel Shear schematic is overlaid on the rose diagram of trends in the long axes of high confidence, elliptical features, R aligns closely with the primary NE trend (**Fig. 23A**). When the same schematic of overlaid on the rose diagram of trends in linear arrays, the primary NE trend matches R very closely (**Fig. 23B**). When a Riedel Shear schematic is overlaid on a satellite image of Mt Marsabit, the trend of R is also very close to the NE trending belts of the volcanic field (**Fig. 23C**). Magmatic conduits exploiting en-echelon R shear deformation zones would produce dikes with trends reflected in the shape and distribution of volcanic centers on Mt Marsabit.

6.5.1 Model Limitations

While the trends of R and the trend of linear arrays are very similar, two factors cast doubt on this proposed model.

Firstly, there is no evidence of R’ shears in the vicinity of Mt Marsabit. No cone or crater examined in the morphology analysis displays a trend close to the assumed trend of R’. Additionally, only one trend is observed in linear arrays, which mirrors the assumed trend of R. Future fieldwork and geophysical studies could be key in revealing or disproving the presence of R’ shears.

Secondly, the proposed model does not explain secondary E-W and N-S trends identified in the morphology analysis. These secondary trends are most prominent on the summit and immediately west of the summit (Clusters KD.1 and KD.1) and within the outcrop of the Korr Complex to the SW of the mountain (KD.6). Further study is needed to find the controlling factor in these secondary populations.

7 Conclusion

Two analyses were performed to identify trends on Mt Marsabit: the shapes of features (morphology) and the distribution of those features. 185 volcanic centers met the morphology analysis criteria, and when considered as a whole, display a strong NE trend and secondary N-S and E-W trends (**Fig. 15**). When examined geographically using two different clustering techniques, it appears that these secondary trends are constrained by location: the summit and northeast extent of the volcanic field display prominent NE trends, where N-S and E-W trends are prominent in the northwest and southwest extent (**Figs. 17 and 18**). Examining linear arrays identified in the 3-point alignment code reveals an exclusive NE trend.

This variety of trends could not be produced by pure E-W extension in the Turkana Depression. A combination of controls can best explain our observations: the stress field east of Lake Turkana is locally rotated and is not purely extensional. In the formation of the Mt Marsabit volcanic field, subsurface feeder dikes exploited weaknesses in the lithosphere resulting in the different populations of trends we see today. If these weaknesses are a product of Riedel shears, then this environment is also affected by strike-slip motion and is not purely extensional.

This project has accomplished goals outside of determining the controlling factors on dike propagation in the Mt Marsabit volcanic field, and possibly the eastern Turkana Depression. The results add to a growing number of studies that use code to identify three-point alignments in volcanic features. Volcanic lineaments have been historically difficult to identify. Early studies manually drew alignments between center points of volcanic features (Nakamura, 1977) - a practice fraught with ambiguities. This method produced linear arrays that were difficult to duplicate and not supported by geological settings. Other studies still manually draw alignments, but only between elongated features (Paulsen and Wilson, 2010). This method still leaves too much to human interpretation and again resulted in linear arrays that are not reproducible. This study adds valuable evidence that Le Corvec’s three-point alignment code produces repeatable, accurate trends for linear arrays without human error or interpretation biases.

Remote sensing and GIS have allowed us to perform an in-depth geo-spatial analysis on the other side of the world using easily accessible tools. Geology has long been a field limited to those with the ability and means to dedicate weeks in the field under sometimes grueling conditions. Field camp, a requirement in most universities for a geology degree, requires students to take substantial time off from work and family duties and spent hundreds, if not thousands, of dollars on airfare, field gear, and tuition. These restrictions have limited the pool of potential geologists. The Covid-19 pandemic of 2020 forced many schools to consider how to teach geologic principles remotely. Remote sensing and GIS are invaluable tools that can bring geology to a wider audience.

Works Cited

Ahlgren, S.G., 2001. The nucleation and evolution of Riedel shear zones as deformation bands in porous sandstone. Journal of Structural Geology, 23(8), pp.1203-1214.

Allmendinger, R. W., Cardozo, N. C., and Fisher, D., 2013, Structural Geology Algorithms: Vectors & Tensors: Cambridge, England, Cambridge University Press, 289 pp.

Anderson, E.M., 1905. The dynamics of faulting. Transactions of the Edinburgh Geological Society, 8(3), pp.387-402.

Beggan, C., and Hamilton, C.W., 2010. New image processing software for analyzing object size-frequency distributions, geometry, orientation, and spatial distribution. Computers & Geosciences, 36(4), pp.539-549.

Blatt, H., and Tracy, R.J., 1996. Petrology: igneous, sedimentary, and metamorphic (2nd ed.). New York: W.H. Freeman. ISBN 0716724383.

Bosworth, W. and Strecker, M.R., 1997. Stress field changes in the Afro-Arabian rift system during the Miocene to Recent period. Tectonophysics, 278(1-4), pp.47-62.

Brune, S., Corti, G. and Ranalli, G., 2017. Controls of inherited lithospheric heterogeneity on rift linkage: Numerical and analog models of interaction between the Kenyan and Ethiopian rifts across the Turkana depression. Tectonics, 36(9), pp.1767-1786.

Brune, S., Kolawole, F., Olive, J.A., Stamps, D.S., Buck, W.R., Buiter, S.J., Furman, T. and Shillington, D.J., 2023. Geodynamics of continental rift initiation and evolution. Nature Reviews Earth & Environment, pp.1-19.

Cardozo, N., and Allmendinger, R. W., 2013, Spherical projections with OSXStereonet: Computers & Geosciences, v. 51, no. 0, p. 193 - 205, doi: 10.1016/j.cageo.2012.07.021

Chorowicz, J., 2005. The East African rift system. Journal of African Earth Sciences (2005), v. 43, p. 379-410.

Clark, P.J., Evans, F.C., 1954. Distance to nearest neighbor as a measure of spatial relationships in populations. Ecology 35 (4), 445–453.

de Silva, S., and Lindsay, J.M., 2015, Primary Volcanic Landforms. In Houghton, B., McNutt, S.R., Rymer, H., Sigurdsson, H., and Stix, J., eds., The Encyclopedia of Volcanoes (second edition): Amsterdam, Netherlands, Academic Press, p. 273-320.

DeMets, C., and S. Merkouriev (2016), High-resolution estimates of Nubia–Somalia plate motion since 20 Ma from reconstructions of the Southwest Indian Ridge, Red Sea and Gulf of Aden, Geophys. J. Int., 207(1), 317–332, doi:10.1093/gji/ggw276.

Ebinger, C., 2005. Continental break-up: the East African perspective. *Astronomy & Geophysics*, *46*(2), pp.2-16.

Ebinger, C.J., Yemane, T., Harding, D.J., Tesfaye, S., Kelley, S. and Rex, D.C., 2000. Rift deflection, migration, and propagation: Linkage of the Ethiopian and Eastern rifts, Africa. *Geological Society of America Bulletin*, *112*(2), pp.163-176.

Etheridge, M.A., 1983. Differential stress magnitudes during regional deformation and metamorphism: upper bound imposed by tensile fracturing. Geology, 11(4), pp.231-234.

Fernandes, R.M.S., Ambrosius, B.A.C., Noomen, R., Bastos, L., Combrinck, L., Miranda, J.M. and Spakman, W., 2004. Angular velocities of Nubia and Somalia from continuous GPS data: implications on present-day relative kinematics. Earth and Planetary Science Letters, 222(1), pp.197-208.

Franceschini, Z., Cioni, R., Scaillet, S., Corti, G., Sani, F., Isola, I., Mazzarini, F., Duval, F., Erbello, A., Muluneh, A. and Brune, S., 2020. Recent volcano-tectonic activity of the Ririba rift and the evolution of rifting in South Ethiopia. Journal of Volcanology and Geothermal Research, 403, p.106989.

Franceschini, Z., Cioni, R., Scaillet, S., Corti, G., Sani, F., Isola, I., Mazzarini, F., Duval, F., Erbello, A., Muluneh, A. and Brune, S., 2020. Recent volcano-tectonic activity of the Ririba rift and the evolution of rifting in South Ethiopia. Journal of Volcanology and Geothermal Research, 403, p.106989.

Gonnermann, H., and Taisne, B., 2015, Magma Transport in Dikes. In Houghton, B., McNutt, S.R., Rymer, H., Sigurdsson, H., and Stix, J., eds., The Encyclopedia of Volcanoes (second edition): Amsterdam, Netherlands, Academic Press, p. 273-320.

Hobbs, B.E., Ord, A. and Regenauer-Lieb, K., 2011. The thermodynamics of deformed metamorphic rocks: a review. Journal of Structural Geology, 33(5), pp.758-818.

Iaffaldano, G., R. Hawkins, and M. Sambridge (2014), Bayesian noise-reduction in Arabia/Somalia and Nubia/Arabia finite rotations since ∼20 Ma: Implications for Nubia/Somalia relative motion, Geochem. Geophys. Geosyst., 15, 845–854, doi:10.1002/2013GC005089.

Isola, I., Mazzarini, F., Bonini, M. and Corti, G., 2014. Spatial variability of volcanic features in early-stage rift settings: the case of the Tanzania Divergence, East African rift system. Terra Nova, 26(6), pp.461-468.

Key, R., 1987. Geology of the Marsabit area. Degree sheet 20 with coloured 1: 25 000 geological map and results of geochemical exploration.

Key, R.M., Rop, B.P. and Rundle, C.C., 1987. The development of the late Cenozoic alkali basaltic Marsabit shield volcano, northern Kenya. Journal of African Earth Sciences (1983), 6(4), pp.475-491.

Key, R.M., Charsley, T.J., Hackman, B.D., Wilkinson, A.T. and Rundle, C.C., 1989. Superimposed upper Proterozoic collision-controlled orogenies in the Mozambique orogenic belt of Kenya. Precambrian Research, 44(3-4), pp.197-225.

Koehn, D., Aanyu, K., Haines, S. and Sachau, T., 2008. Rift nucleation, rift propagation and the creation of basement micro-plates within active rifts. Tectonophysics, 458(1-4), pp.105-116.

LaFemina, P.C., 2015. Plate tectonics and volcanism. In Houghton, B., McNutt, S.R., Rymer, H., Sigurdsson, H., and Stix, J., eds., The Encyclopedia of Volcanoes (second edition): Amsterdam, Netherlands, Academic Press, p. 65-92.

Le Corvec, N., Menand, T. and Lindsay, J., 2013a. Interaction of ascending magma with pre-existing crustal fractures in monogenetic basaltic volcanism: an experimental approach. Journal of Geophysical Research: Solid Earth, 118(3), pp.968-984.

Le Corvec, N., Spörli, K.B., Rowland, J. and Lindsay, J., 2013b. Spatial distribution and alignments of volcanic centers: clues to the formation of monogenetic volcanic fields. Earth-Science Reviews, 124, pp.96-114.

Macgregor, D., 2015. History of the development of the East African Rift System: A series of interpreted maps through time. Journal of African Earth Sciences, 101, pp.232-252.

Mana, S., Furman, T., Turrin, B.D., Feigenson, M.D. and Swisher III, C.C., 2015. Magmatic activity across the East African North Tanzanian divergence zone. Journal of the Geological Society, 172(3), pp.368-389.

Mazzarini, F., Le Corvec, N., Isola, I. and Favalli, M., 2016. Volcanic field elongation, vent distribution, and tectonic evolution of a continental rift: The Main Ethiopian Rift example. Geosphere, 12(3), pp.706-720.

Mazzarini, F. and Isola, I., 2022. Quaternary off-rift volcanism along a section of the East African Rift System (EARS), from the south Ethiopia to the south Kenya. Italian Journal of Geosciences, 141(3), pp.334-347.

Moore, J. M. 1979. Tectonics of the Najd transcurrent fault system, Saudi Arabia. Journal of the Geological Society of London 136, 441 -454.

Morley, C.K., Bosworth, W., Day, R.A., Lauck, R., Bosher, R., Stone, D.M., Wigger, S.T., Wescott, W.A., Haun, D. and Bassett, N., 1999. AAPG Studies in Geology# 44, Chapter 4: Geology and Geophysics of the Anza Graben.

Muirhead, J.D., Kattenhorn, S.A. and Le Corvec, N., 2015. Varying styles of magmatic strain accommodation across the East African Rift. Geochemistry, Geophysics, Geosystems, 16(8), pp.2775-2795.

Muirhead, J.D., Scholz, C.A. and O. Rooney, T., 2022. Transition to magma-driven rifting in the South Turkana Basin, Kenya: Part 1. Journal of the Geological Society, 179(6), pp.jgs2021-159.

Nakamura, K., 1977. Volcanoes as possible indicators of tectonic stress orientation-principal and proposal. Journal of Volcanology and Geothermal Research 2, 1–16.

Németh, K., 2010. Monogenetic volcanic fields: Origin, sedimentary record, and relationship with polygenetic volcanism. In What Is a Volcano? GSA Special Paper (Vol. 470, p. 43).

Oliva, S.J., Ebinger, C.J., Rivalta, E., Williams, C.A., Wauthier, C. and Currie, C.A., 2022. State of stress and stress rotations: Quantifying the role of surface topography and subsurface density contrasts in magmatic rift zones (Eastern Rift, Africa). Earth and Planetary Science Letters, 584, p.117478.

Paulsen, T.S. and Wilson, T.J., 2010. New criteria for systematic mapping and reliability assessment of monogenetic volcanic vent alignments and elongate volcanic vents for crustal stress analyses. Tectonophysics, 482(1-4), pp.16-28.

Ring, U., 1994. The influence of preexisting structure on the evolution of the Cenozoic Malawi rift (East African rift system). Tectonics, 13(2), pp.313-326.

Ring, U., 2014. The East African Rift System. Austrian Journal of Earth Sciences, 107, pp132-146

Ritsema, J., Nyblade, A.A., Owens, T.J., Langston, C.A. and VanDecar, J.C., 1998. Upper mantle seismic velocity structure beneath Tanzania, east Africa: Implications for the stability of cratonic lithosphere. Journal of Geophysical Research: Solid Earth, 103(B9), pp.21201-21213.

Robertson, E.A.M., Biggs, J., Cashman, K.V., Floyd, M.A. and Vye-Brown, C., 2016. Influence of regional tectonics and pre-existing structures on the formation of elliptical calderas in the Kenyan Rift. Geological Society, London, Special Publications, 420(1), pp.43-67.

Rubin, A.M., 1995. Propagation of magma-filled cracks. Annual Review of Earth and Planetary Sciences 23, 287–336.

Saria, E., E. Calais, D. S. Stamps, D. Delvaux, and C. J. H. Hartnady (2014), Present-day kinematics of the East African Rift, J. Geophys. Res. Solid Earth, 119, 3584–3600, doi:10.1002/2013JB010901.

Stamps, D. S., L. M. Flesch, E. Calais, and A. Ghosh (2014), Current kinematics and dynamics of Africa and the East African Rift System, J. Geophys. Res. Solid Earth, 119, 5161–5186, doi:10.1002/2013JB010717.

Silverman, B.W., 2018. Density estimation for statistics and data analysis. Routledge.

Sippel, J., Meeßen, C., Cacace, M., Mechie, J., Fishwick, S., Heine, C., Scheck-Wenderoth, M. and Strecker, M.R., 2017. The Kenya rift revisited: insights into lithospheric strength through data-driven 3-D gravity and thermal modelling. Solid Earth, 8(1), pp.45-81.

Tanner, W. F. 1962. Surface structural patterns obtained from strike -slip models. Journal of Geology 70, 101 -107.

Turcotte, D.L. and Emerman, S.H., 1983. Mechanisms of active and passive rifting. In Developments in geotectonics (Vol. 19, pp. 39-50). Elsevier.

Valentine, G.A., and Connor, C.B., 2015. Basaltic volcanic fields, in Houghton, B., McNutt, S.R., Rymer, H., Sigurdsson, H., and Stix, J., eds., The Encyclopedia of Volcanoes (second edition): Amsterdam, Netherlands, Academic Press, pp.331-343.

Van Hazinga, C., Sanders, T., Mana, S. and Waddington, G., 2021. Identifying Extrusive Volcanic Features with YOLOv2.

Vink, G.E., Morgan, W.J. and Zhao, W.L., 1984. Preferential rifting of continents: a source of displaced terranes. Journal of Geophysical Research: Solid Earth, 89(B12), pp.10072-10076.

Wang, Y., Zou, Y., Henrickson, K., Wang, Y., Tang, J. and Park, B.J., 2017. Google Earth elevation data extraction and accuracy assessment for transportation applications. PloS one, 12(4), p.e0175756.

Weatherspark, 2019, Average Weather in Marsabit Kenya: https://weatherspark.com/y/100146/Average-Weather-in-Marsabit-Kenya-Year-Round, Accessed Nov 1, 2019

White, J.D. and Ross, P.S., 2011. Maar-diatreme volcanoes: A review. Journal of Volcanology and Geothermal Research, 201(1-4), pp.1-29.

Wilcox, R. E., Harding, T. P. & Seely, D. R. 1973. Basic wrench tectonics. The American Association of Petroleum Geologists Bulletin 57(1), 74 -96.

Williams L.A.J. (1970) - The volcanics of the gregory rift valley, east Africa. Bull. Volcanol., 34, 439-465, https://doi.org/10.1007/BF02596767.

Windfinder, 2023, Wind and Weather Forecast: Marsabit: https://www.windfinder.com/forecast/marsabit_marsabit_kenya, Accessed Feb 24, 2023

Figures

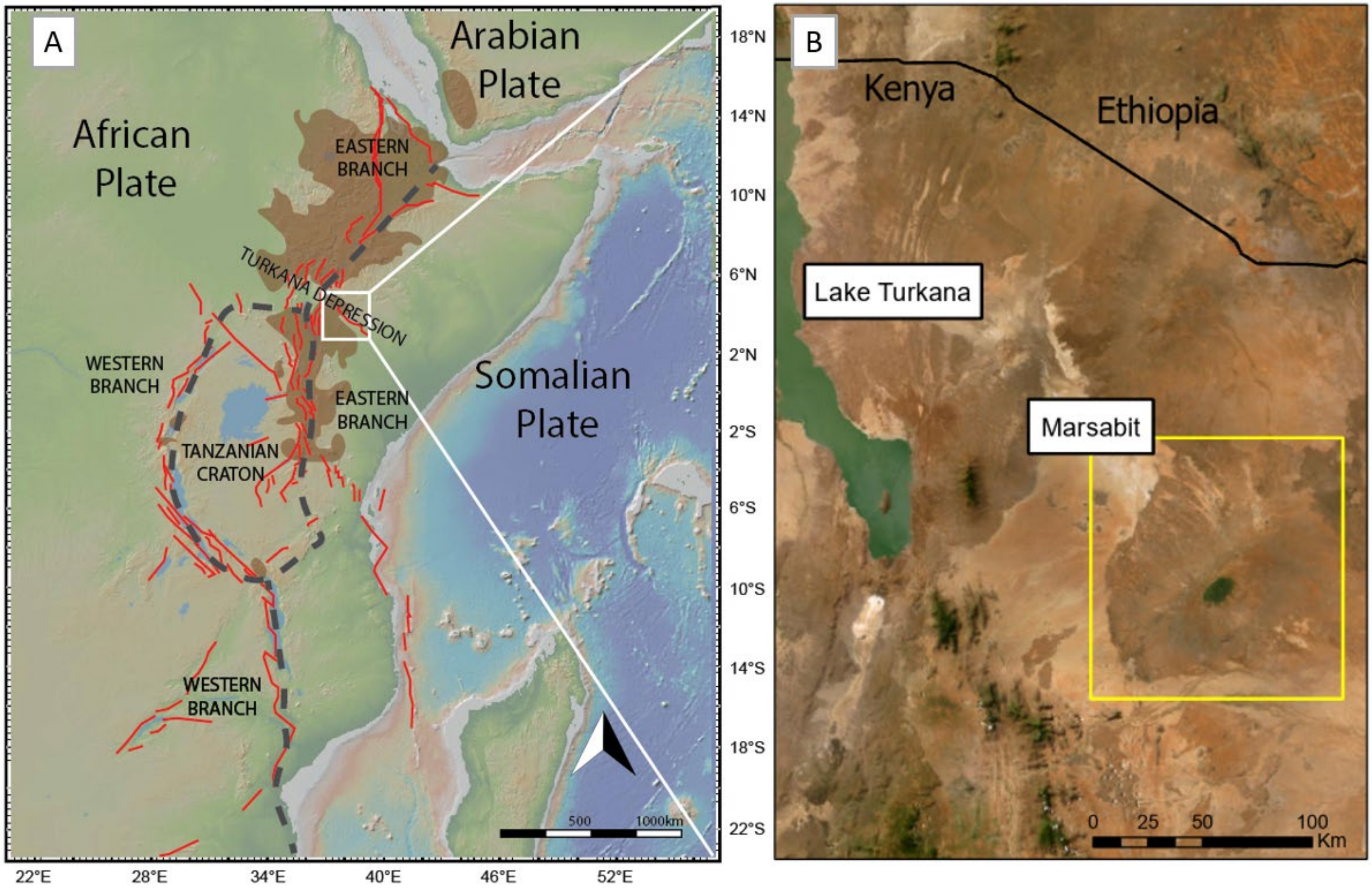

Figure 1 *A) The East African Rift. Red lines indicate Miocene to Holocene major faults, dashed blue lines indicate plate boundaries, and brown indicates the extent of magmatism. Adapted from Mana et al. (2015). (B) Mt Marsabit in the context of southern Ethiopia and northern Kenya*

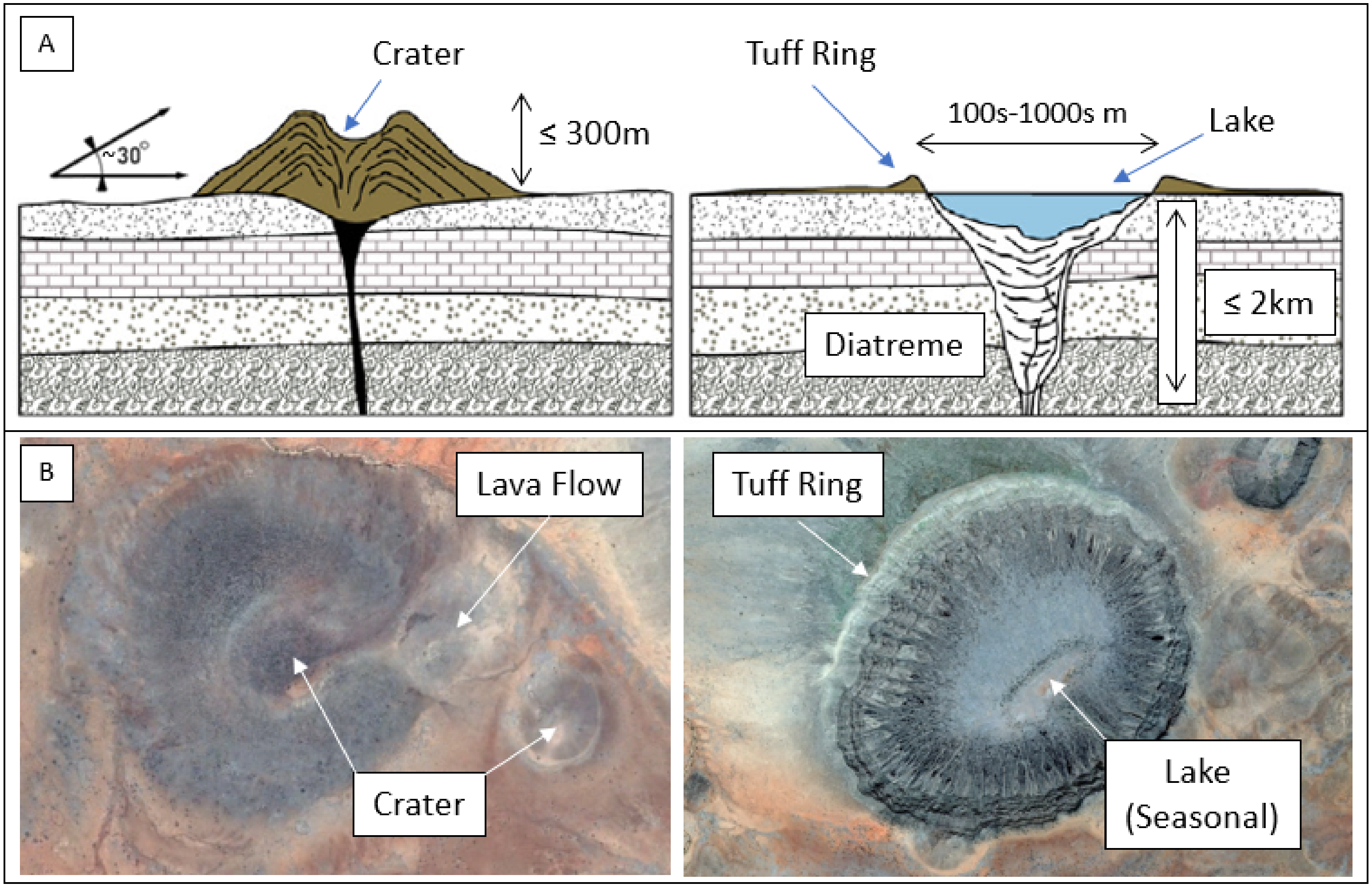

Figure 2 *A) Diagrams illustrating cross cuts of scoria cones (left) and maar craters (right). Adapted from de Silva and Lindsay (2015). B) Satellite images of two scoria cones (left) and a maar crater (right) in the Mt Marsabit Volcanic Field.*

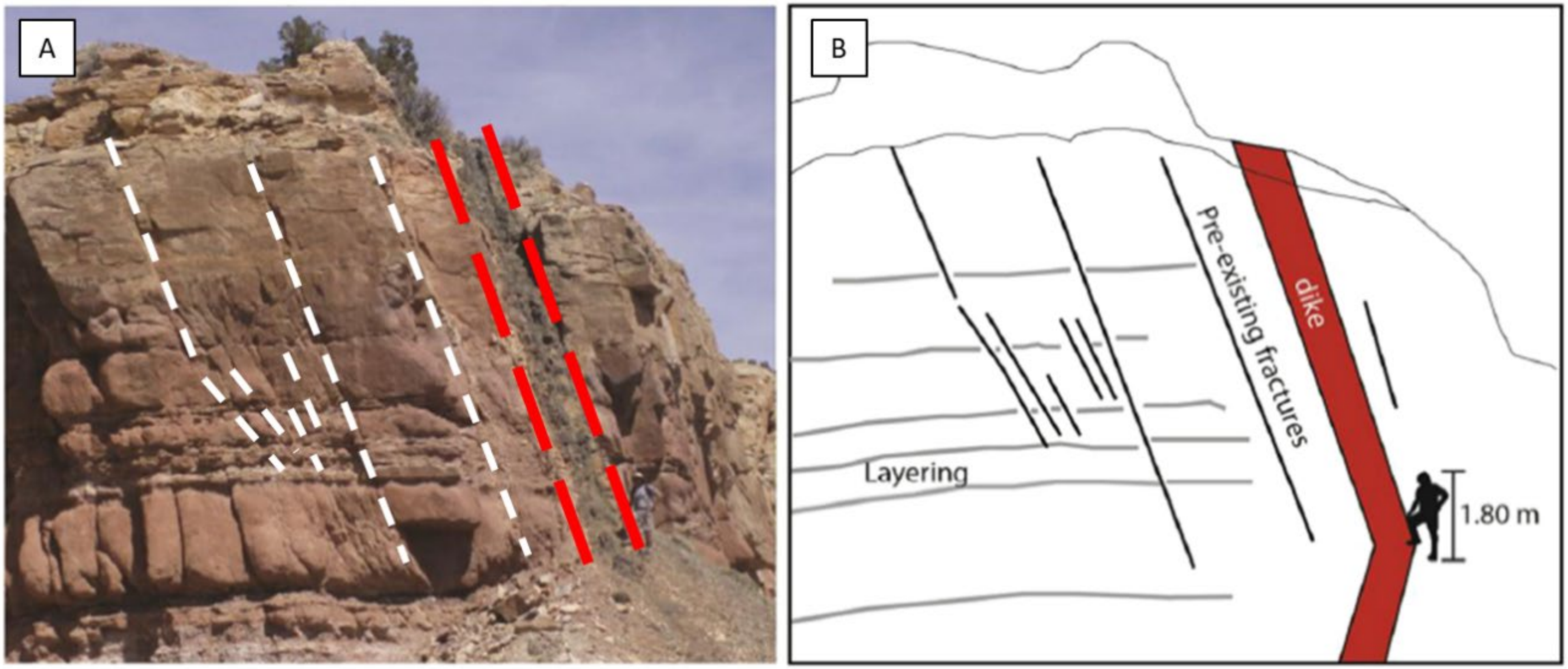

Figure 3 *A) Photograph of fractures (white) and a dike (red) cross cutting sedimentary layers in Utah, USA. B) Cartoon demonstrating the parallel dips of the dike and pre-existing fractures. Modified from LeCorvec et al. (2013a).*

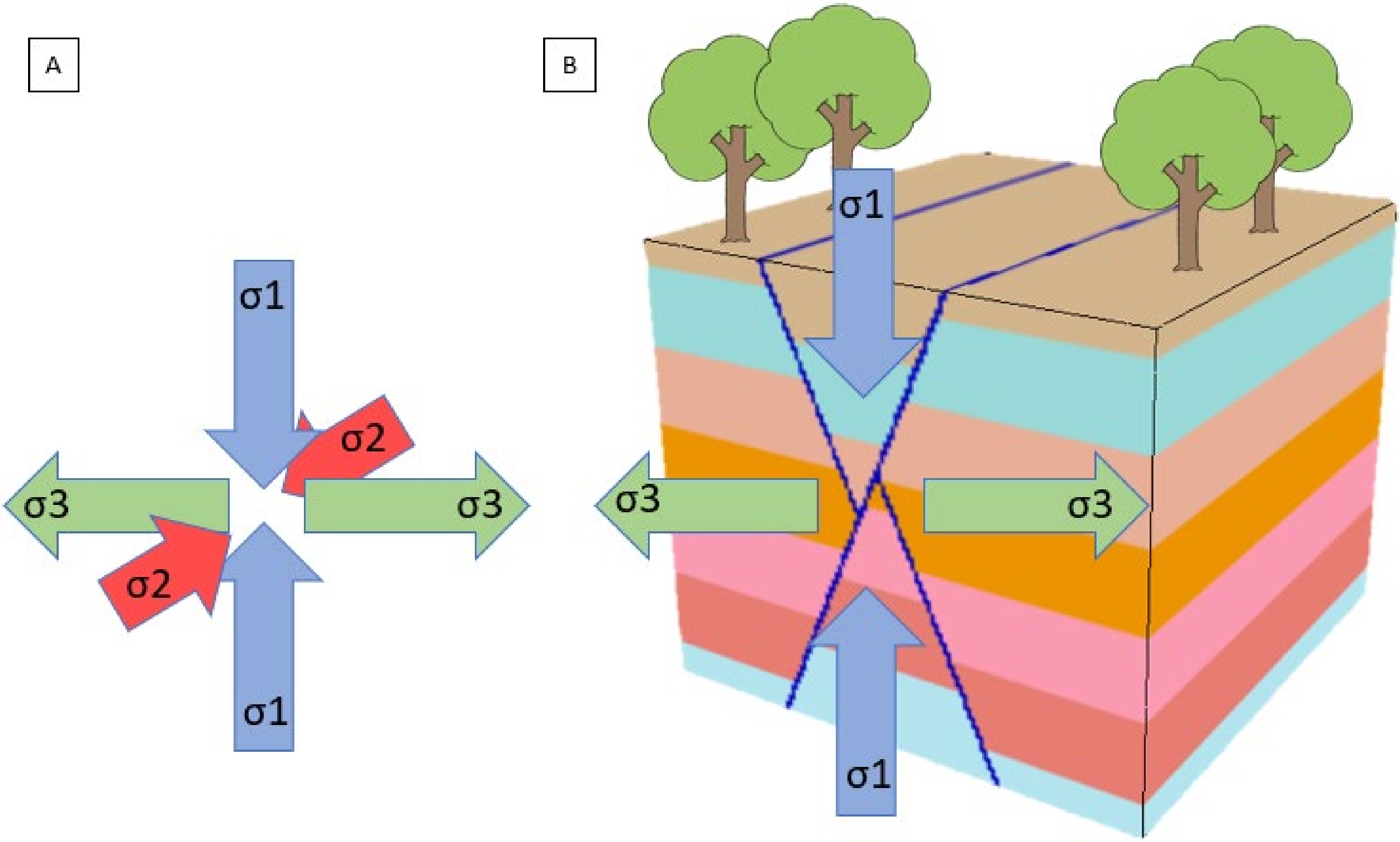

Figure 4 *Cartoon demonstrating Anderson's theory of faulting in an extensional environment. A) σ1 is the direction of maximum compressive stress; σ2 is the direction of intermediate stress; and σ3 is the direction of minimum stress. σ3 is negative stress, making it extensional. B) Cartoon demonstrating σ1 and σ3 in the context of faulting.*

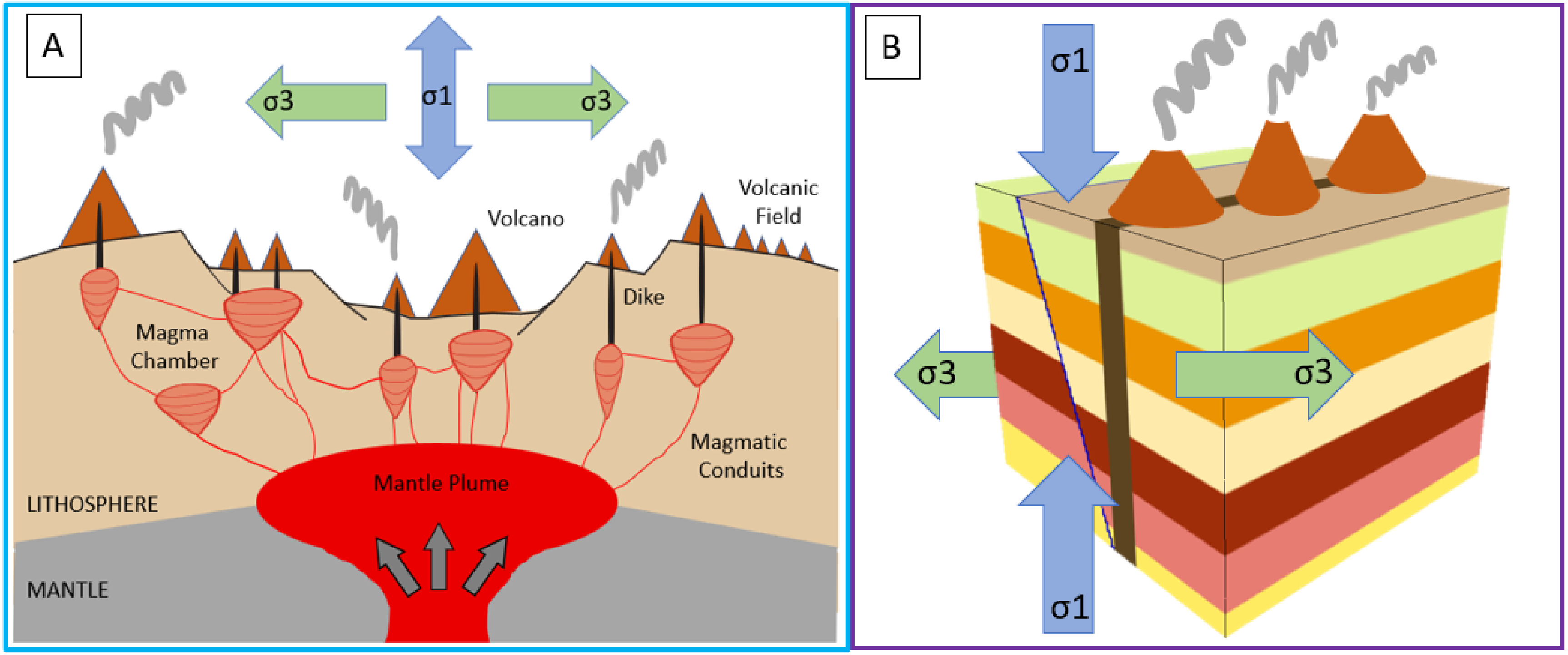

***Figure 5** A) A cartoon simplifying a continental rift like the EAR, fueled by a mantle plume. Magmatic conduits transport lava from the plume to magma chambers, and sometimes directly to volcanoes. Dikes form parallel to σ_1 and perpendicular to σ_3. (B) Anderson's Theory of faulting in a volcanic field in an extensional environment. Note how the dike is parallel to σ_1 and perpendicular to σ_3. Dikes can feed multiple volcanic features, producing cones aligned in a direction consistent with the feeder dike.*

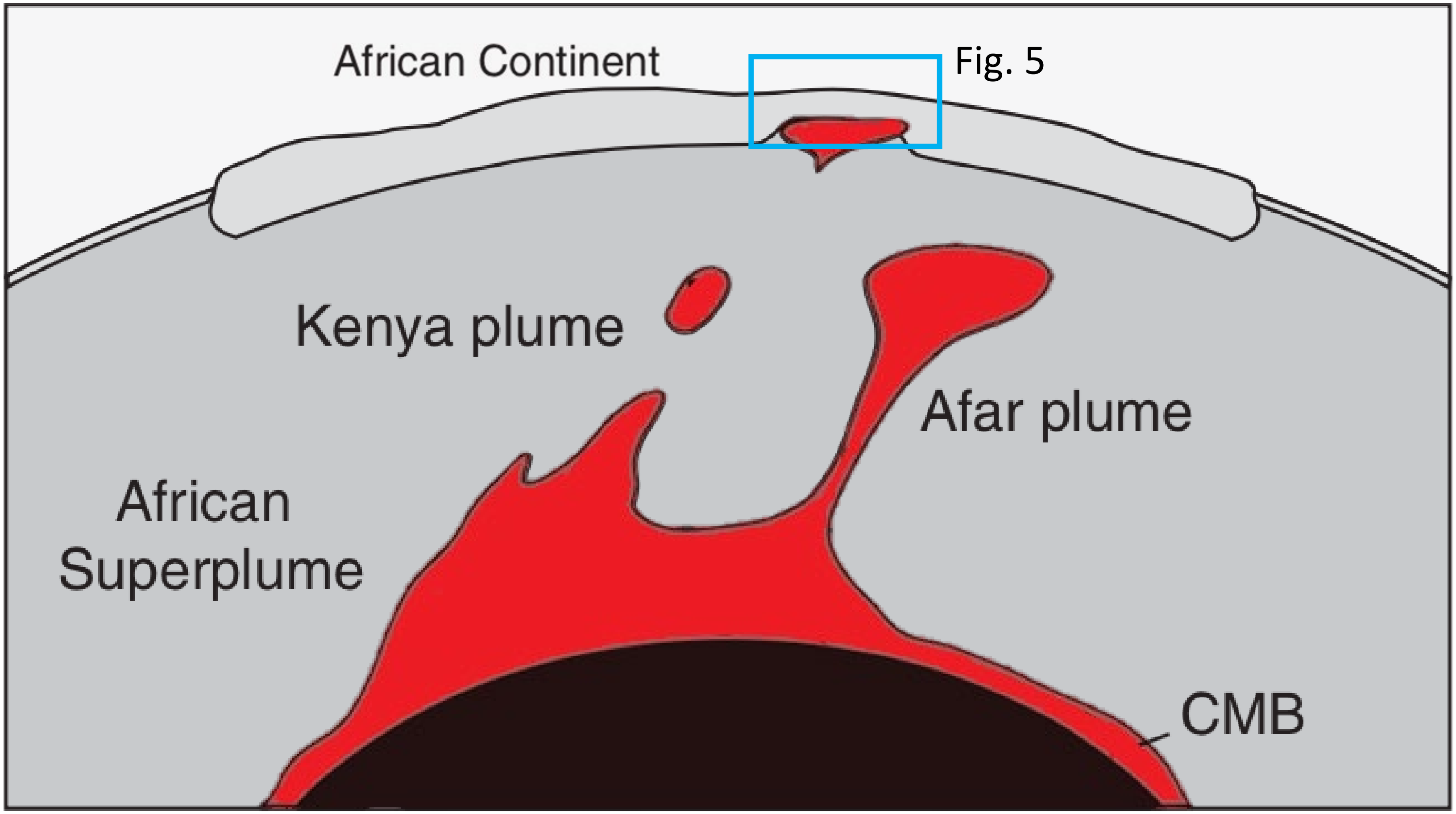

Figure 6 *EAR geodynamic model. It is commonly accepted that one or more mantle plumes are fueling the extension in the EAR. This illustration demonstrates one theory, where smaller plumes have broken off a large superplume. Adapted from Nelson et al. (2012)*

Color	Location	Method	Trend	Ref
🟪	Marsabit	Morphology	035	this study
🟦	Marsabit	Linear Arrays	043	this study
🟥	Marsabit	PCA	036	*Mazzarini et al., 2022*
	Mega	PCA	015	*Franchescini et al., 2020*
	Hurri Hills	PCA	024	*Mazzarini et al., 2022*
	Dilo	PCA	047	*Franchescini et al., 2020*
🟪	South Island	Morphology	007	*Muirhead et al., 2022*
🟨	The Barrier	Faults	012	*Muirhead et al., 2022*
	Buluk Fault Zone	Faults	050	*Vétel and Le Gall, 2006*
	Kataboi Fault Zone	Faults	050	*Vétel and Le Gall, 2006*
	N'Doto Fault Zone	Faults	140	*Vétel and Le Gall, 2006*
⬛	Main Faults	Faults		*Chorowicz 2005*

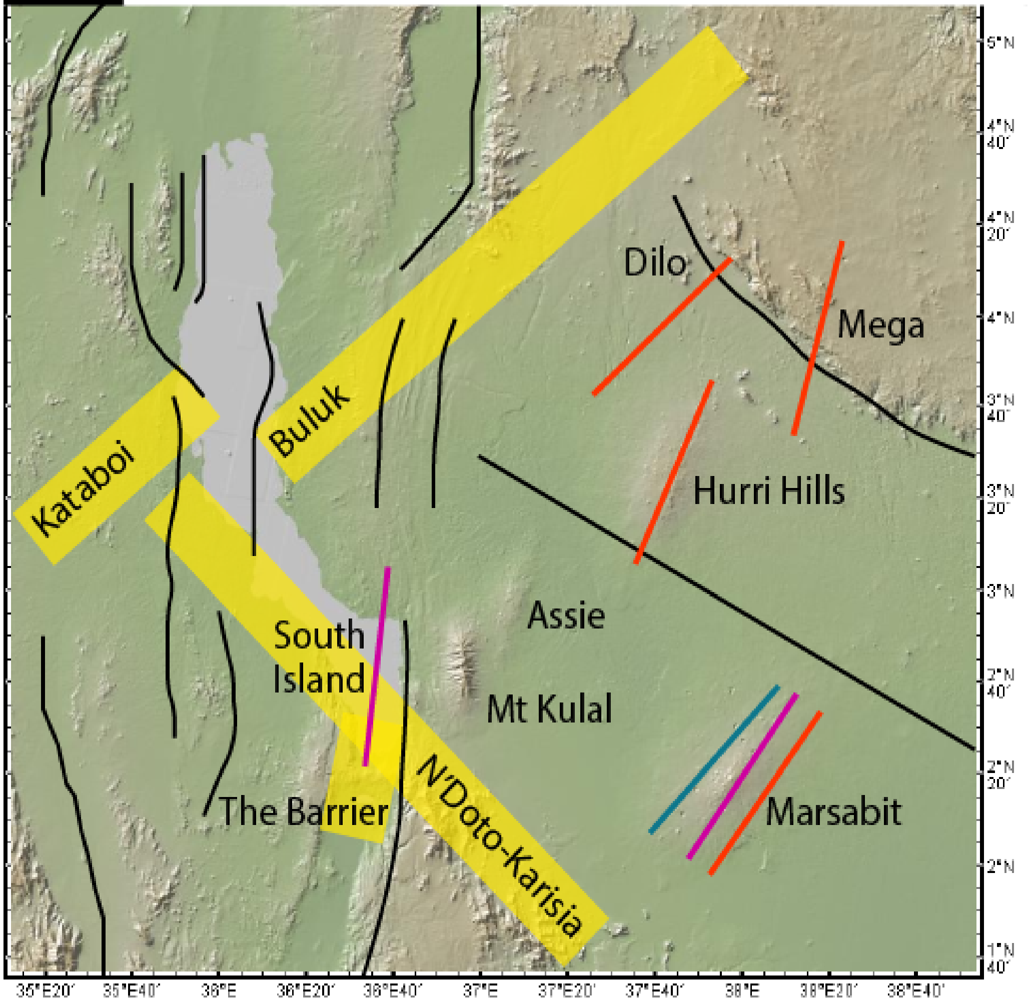

***Figure 7** Trends of volcanic features and faults in East Turkana.*

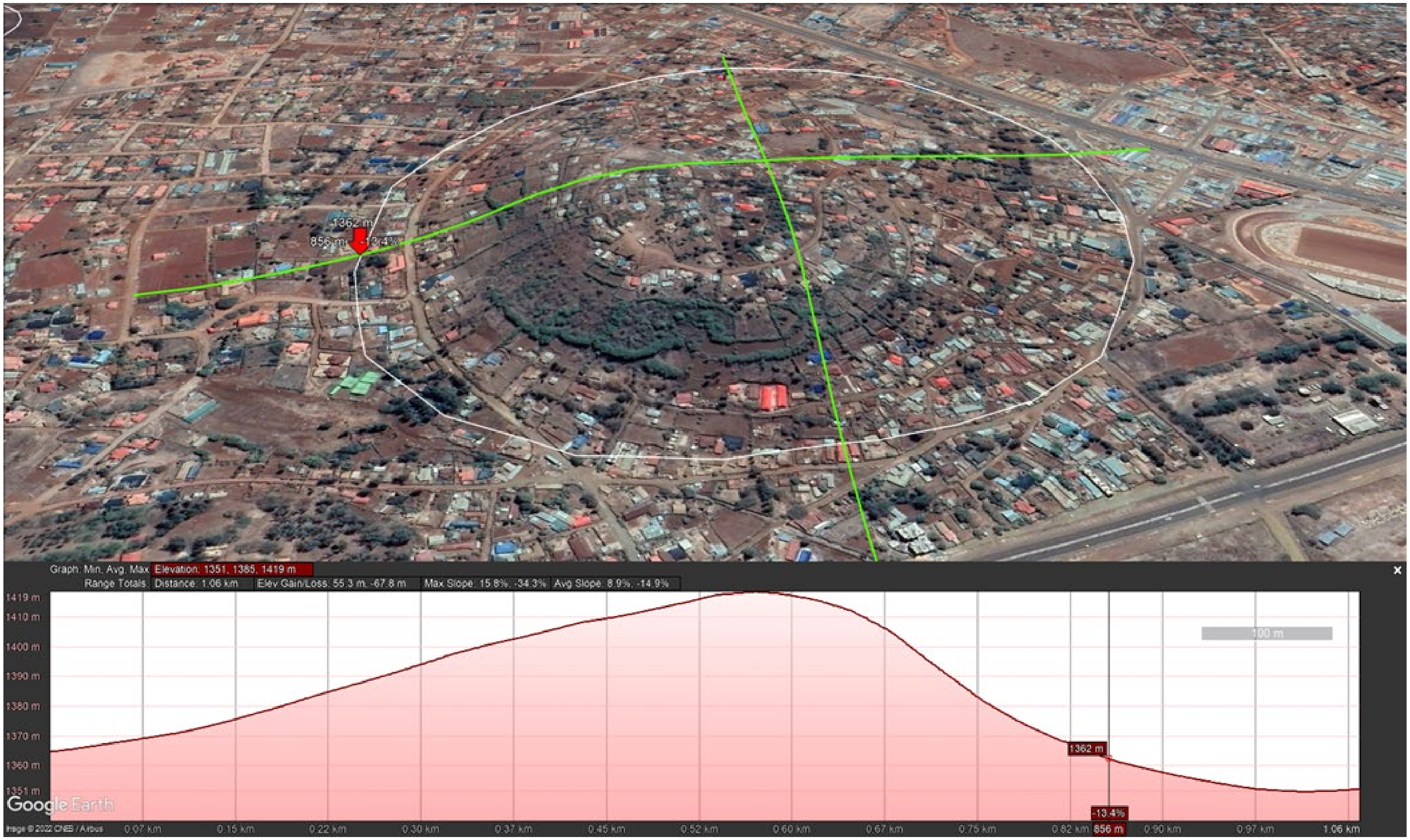

Figure 8 *An example of a cone in the town of Marsabit. Elevation paths help identify the extent of the feature, which is otherwise obscured.*

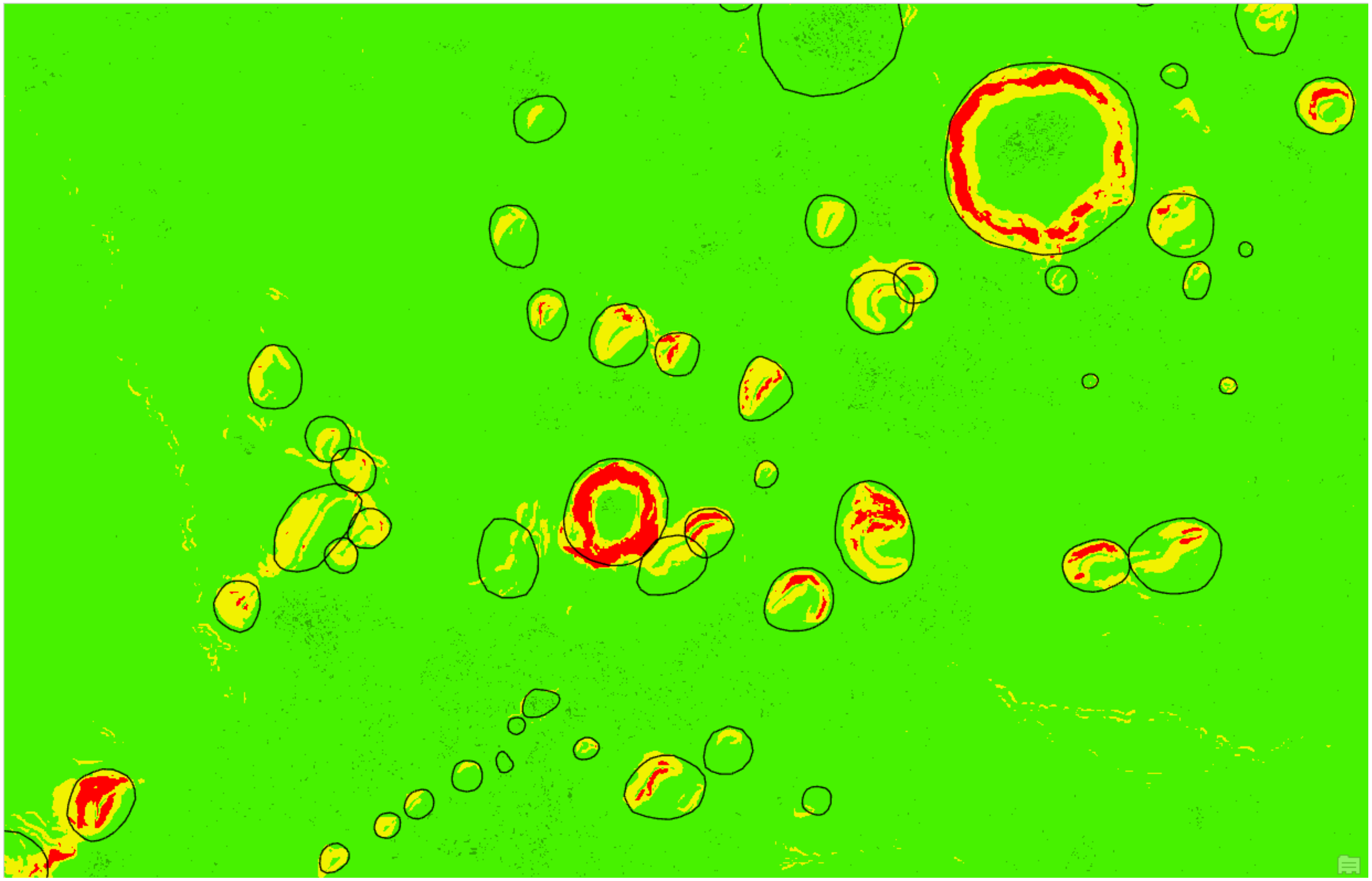

Figure 9 *An example of a DTM from the Nyambeni Hills, a volcanic field located 200km south of Mt Marsabit.*

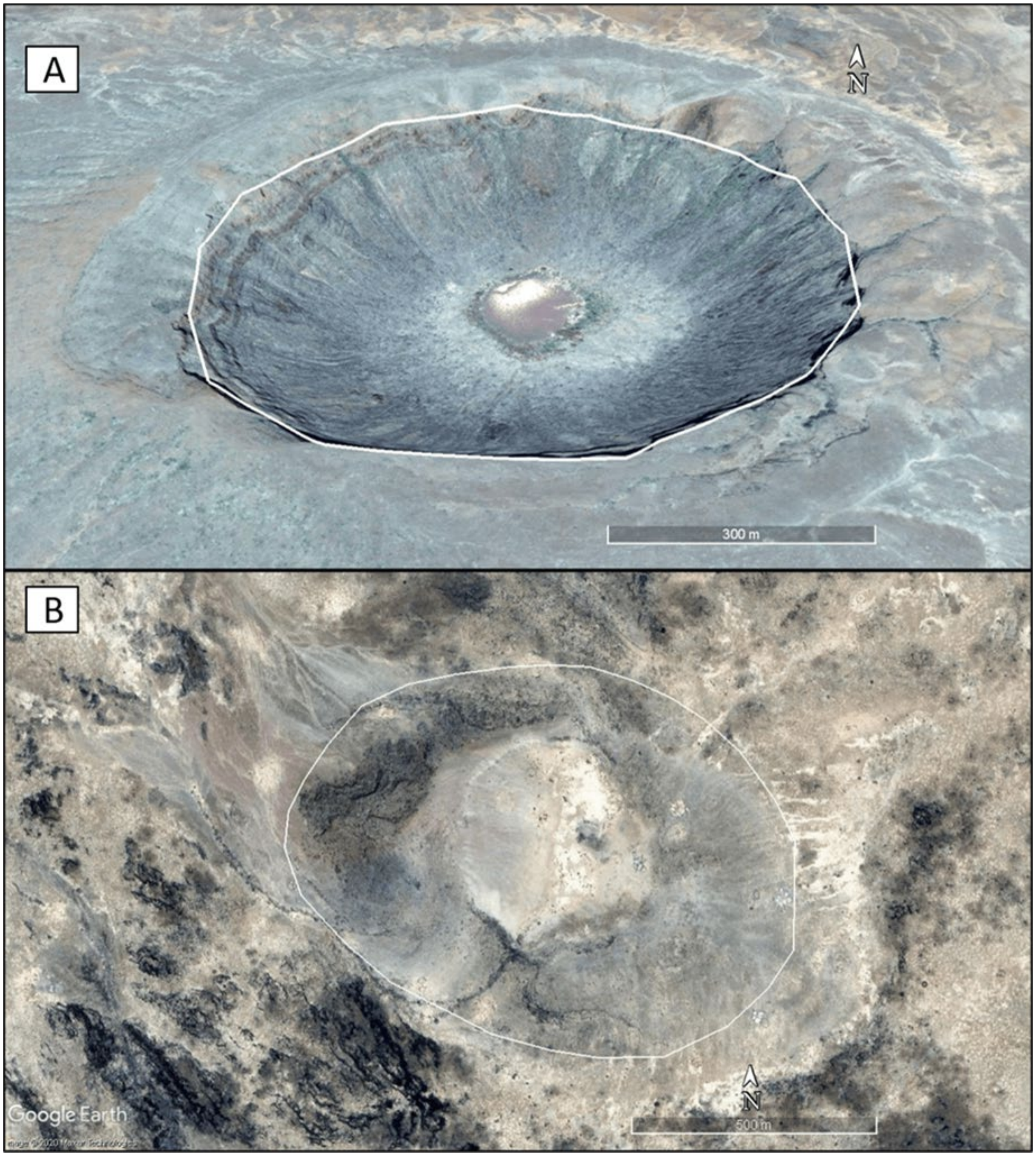

Figure 10 *A) An example of a maar assigned a high confidence score. The rim is clearly defined and not heavily eroded. The polygon is a reliable indicator of the true extent of the maar. B) An example of a cone assigned a low confidence score. This feature is highly eroded, and the original shape of the cone is unclear, and a best fit ellipse was used. Because of the high level of erosion, the polygon is not a reliable indicator of the extent of the cone.*

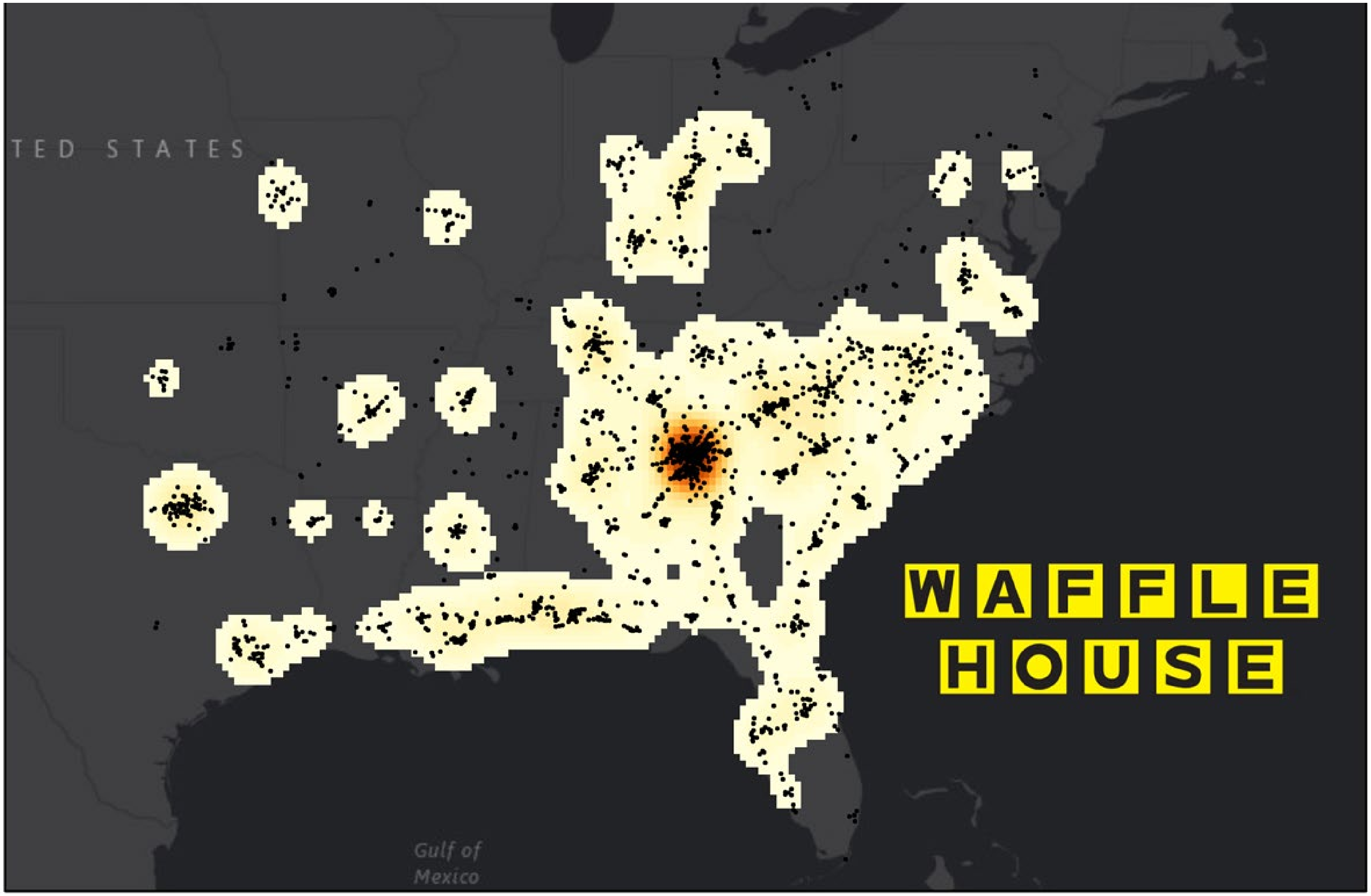

Figure 11 An example of Kernel Density Clusters. Each black spot represents a Waffle House restaurant. The greatest density is found in Atlanta, GA, USA.

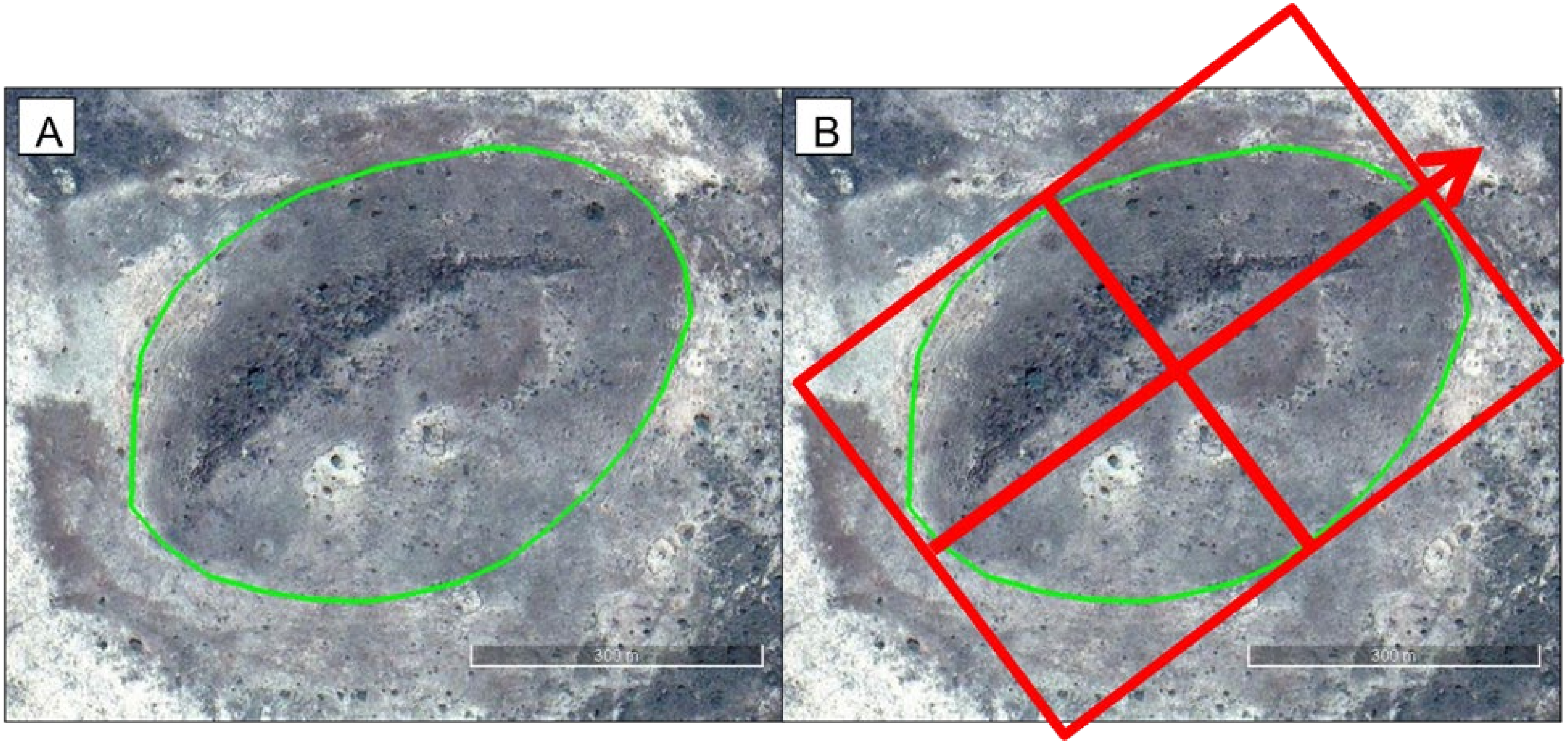

Figure 12 A cartoon demonstrating the Minimum Bounding Geometry tool in ArcGIS Pro.

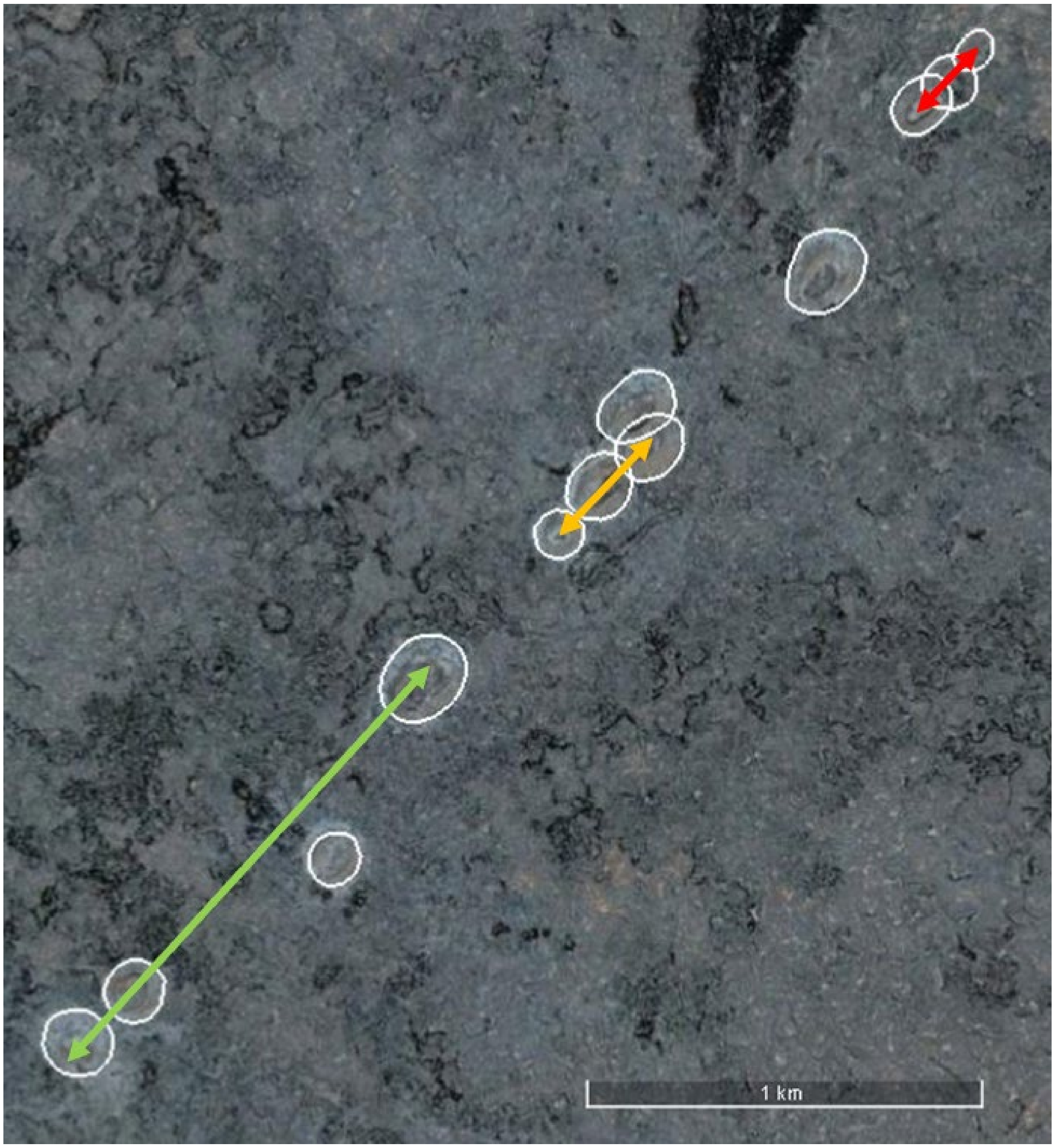

Figure 13 *MATLAB 3-point lineament identification. Three possible linear arrays are indicated here by colored arrows. Each proposed array is a line that crosses the centers of three features. If these lines fall within prescribed width and length tolerances, they will be identified by the MATLAB 3-point alignment script.*

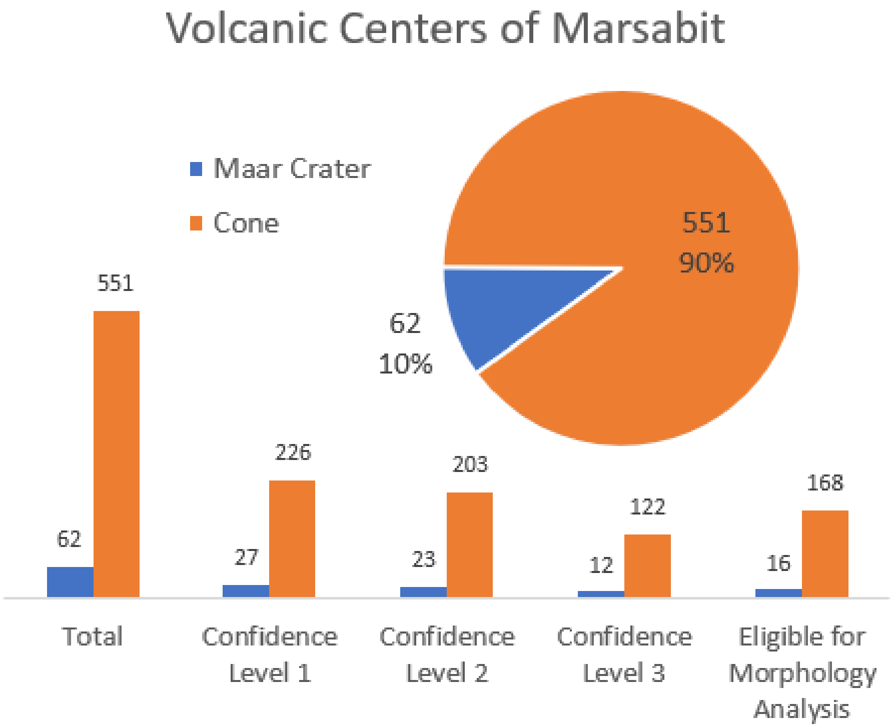

Figure 14 *Feature types and confidence level categories for mapped features. A total of 613 volcanic centers were mapped.*

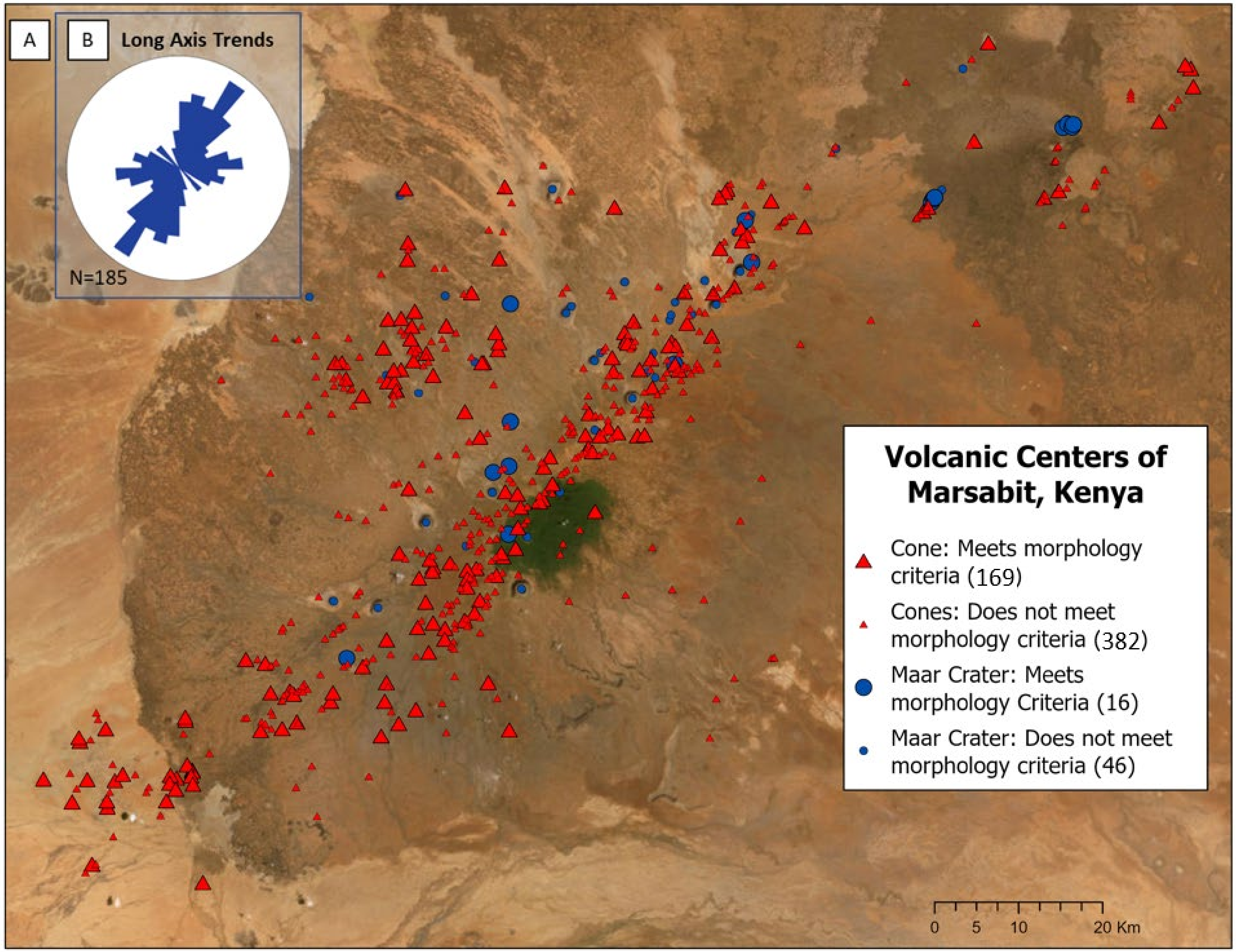

Figure 15 A) Distribution of maar craters, cones, and elliptical high-confidence features used for the morphology analysis. Features meet the criteria if they are elliptical (long/short ratio greater than 1.5) and minimally eroded (CL of 1 or 2). B) Long axis trends of the 185 features that meet morphology analysis criteria.

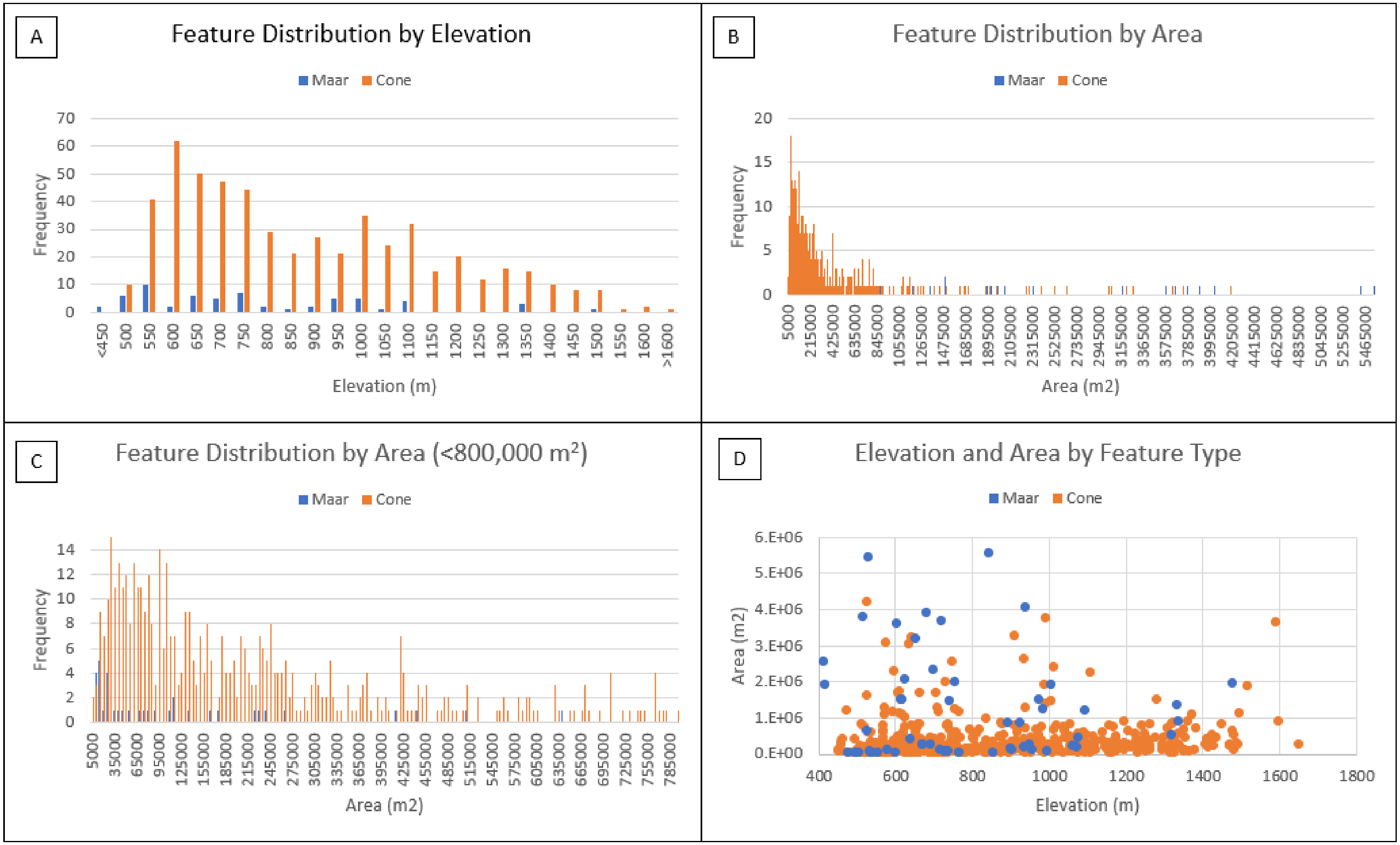

Figure 16 *A comparison between elevation and area of Mt Marsabit volcanic centers. A) Maar craters tend to be smaller in area than craters. Neither cluster at a particular size. B) Most features are less than 800,000 meters sq. C) A closer look at features less than 800,000 meters sq. D) No relationship between elevation and area is apparent.*

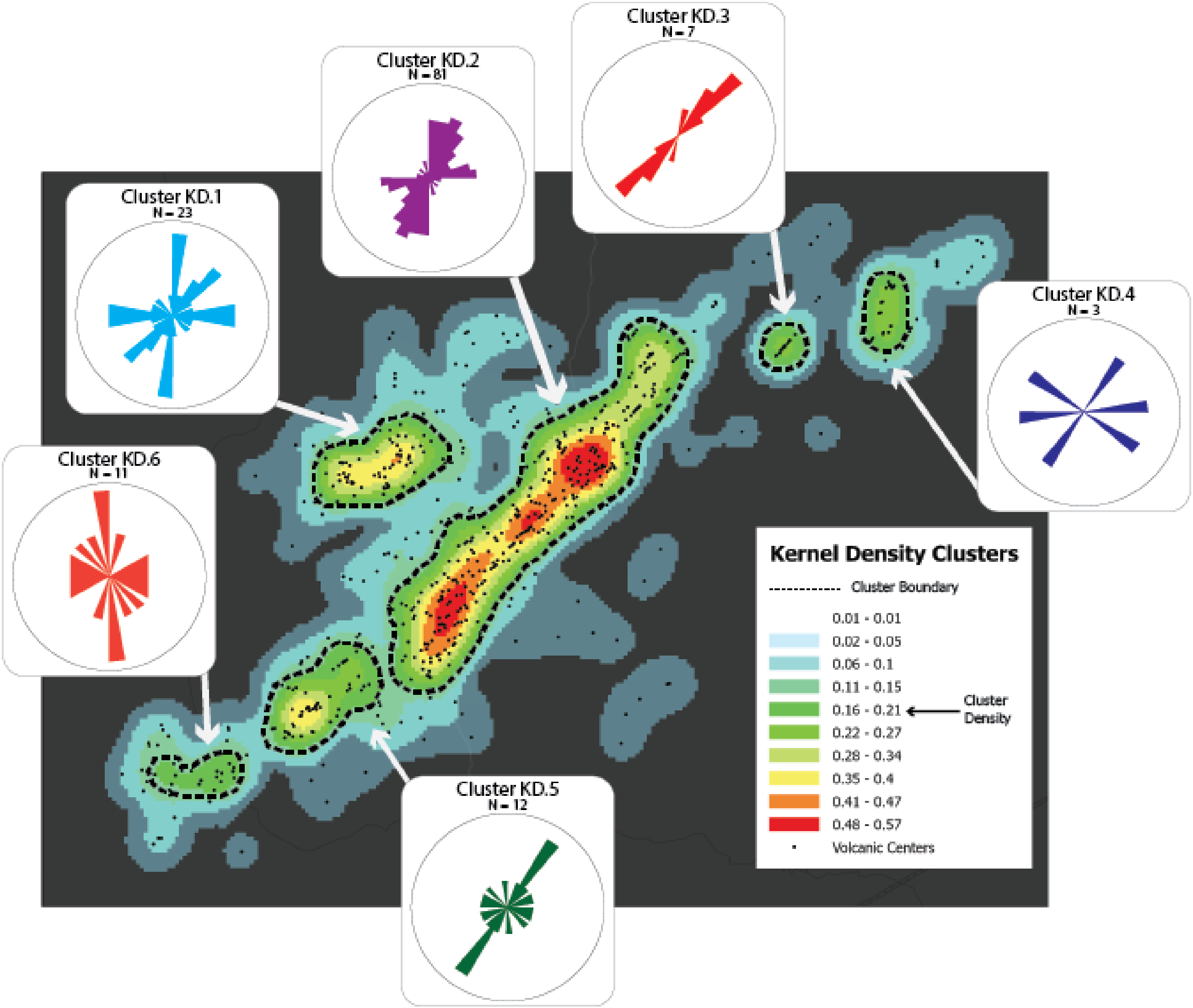

Figure 17 *Six clusters are defined by Kernel Density. Areas with a density greater than 0.16 centers per meter are considered a cluster. Features present below this threshold are disregarded and not included in a cluster.*

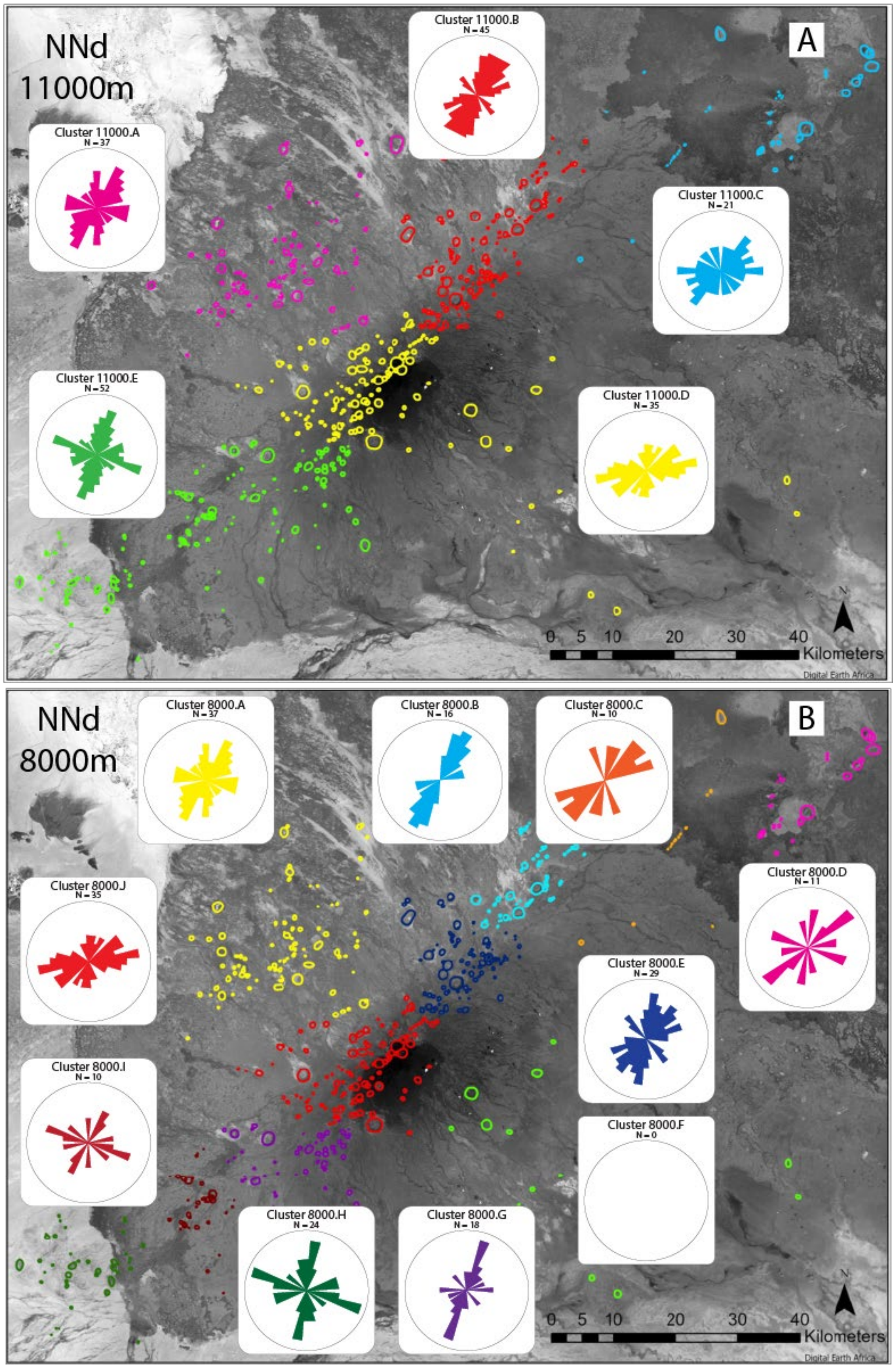

Figure 18 *Clusters defined by Near Neighbor distance (NNd). In this analysis, all features are included in a cluster. A) Clusters are defined by an NNd of 8,000 meters. B) Clusters are defined by an NNd of 11,000 meters.*

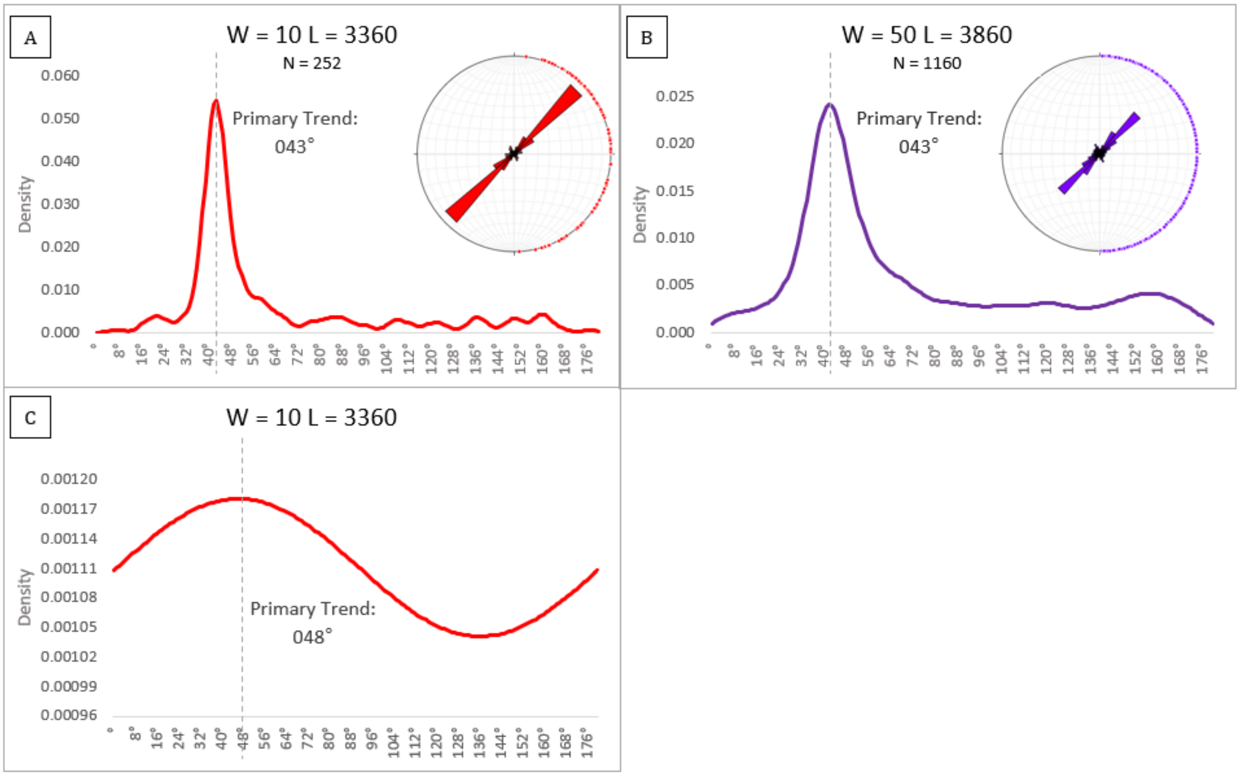

Figure 19 *Histograms of KDE, and rose diagrams of trends for possible linear arrays identified in two different width/length combinations. The value of the rose diagram perimeter is 50%. A) KDE best fit line of the 252 trends identified by the 3-point alignment code within 10m wide and 3360m long thresholds. Note the prominence of the primary trend and the smaller, secondary trends between ~80 and 160°. The rose diagram of the trends reflects the primary trend at 043°. B) KDE best fit line of the 1,160 trends identified by the 3-point alignment code within 50m wide and 3860m long thresholds. While the primary trend is still prominent, most of the secondary trends are not present. The rose diagram reflects the primary trend as well as the reduction of density- this is due to the increase of arrays identified. C) KDE best fit line for trends found within 10m wide and 3360m long thresholds using an extended range from -180 to 360°, zoomed in to 0 to 180°. There is only one visible trend at 048°.*

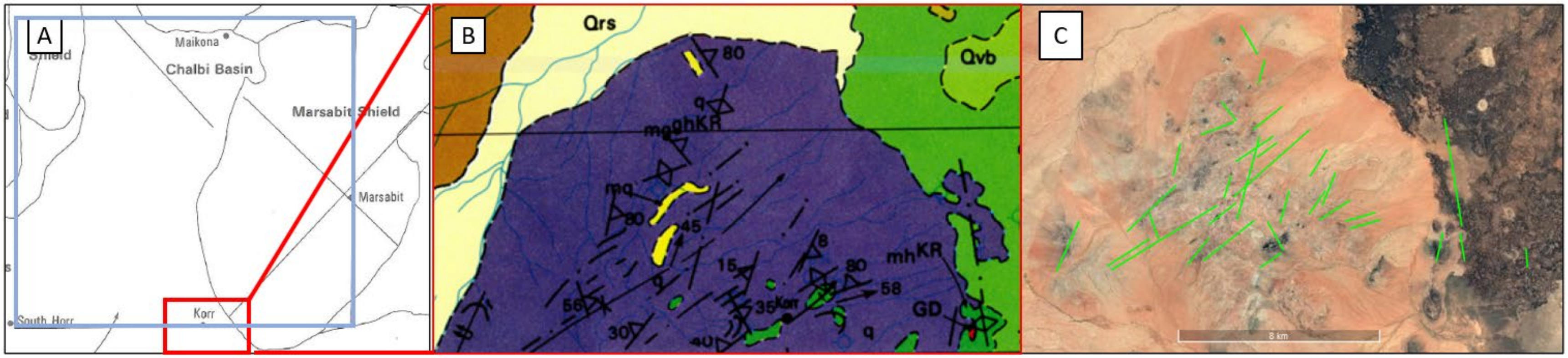

Figure 20 *Selections from Key's map of the Mt Marsabit area (1987). A) The major physiographic provinces of the mapped area. The gray square indicates the extent of the geologic map B) Geologic map of the Korr Hills, to the immediate southwest of Mt Marsabit (Key, 1987). The lines represent the strike of the plane and the gneissosity within the metamorphic Korr Complex. C) Lines from the geologic map drawn in Google Earth Pro and used for basement analyses*

.

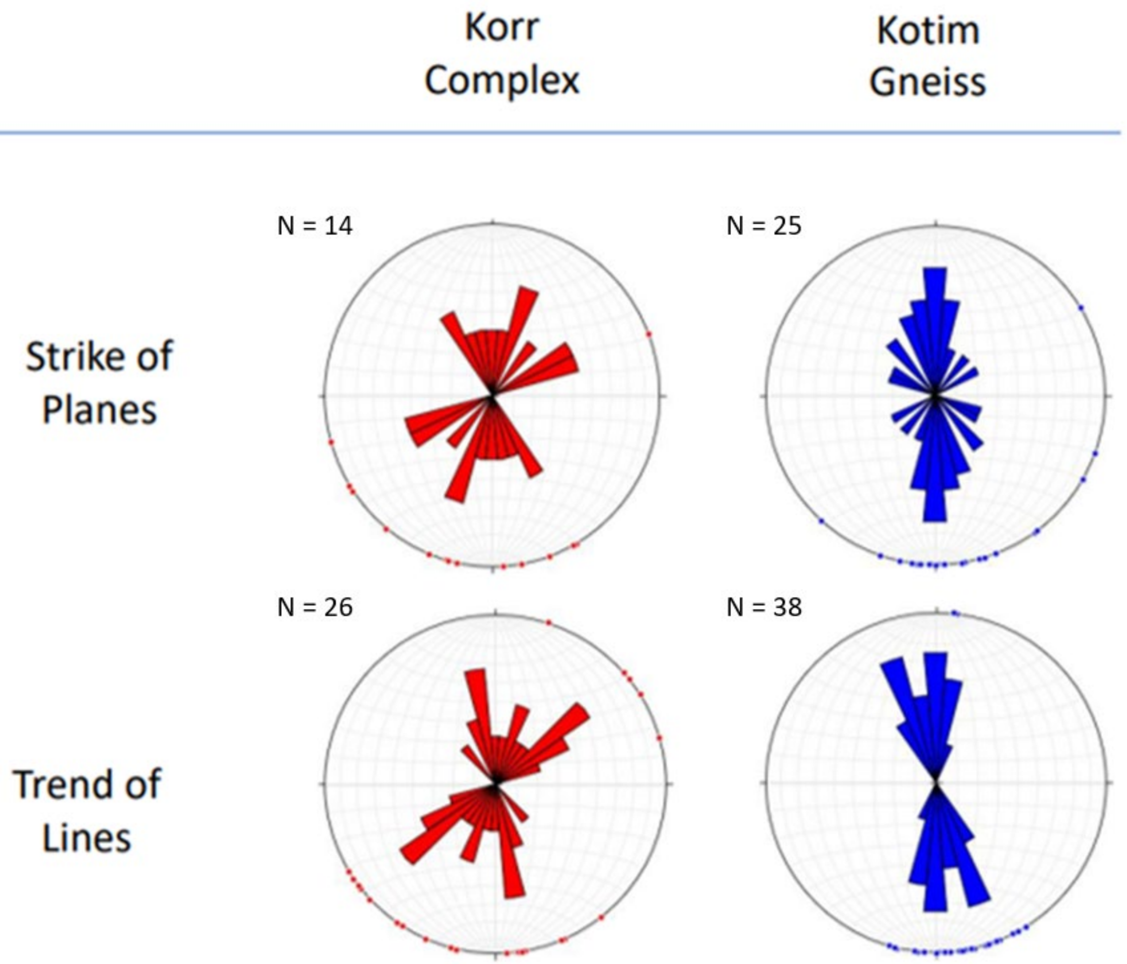

__Figure 21__ Rose Diagrams displaying trends identified in the strike of planes and trend of lines, as mapped by Key (1987), in outcrops of two formations of basement rock: the Korr Complex and Kotim Gneiss (see Fig. 20). The younger, Precambrian Korr Complex displays two primary modes: NWN, N, and NE. The older, also Precambrian Kotim Gneiss displays a strong N-S trend

.

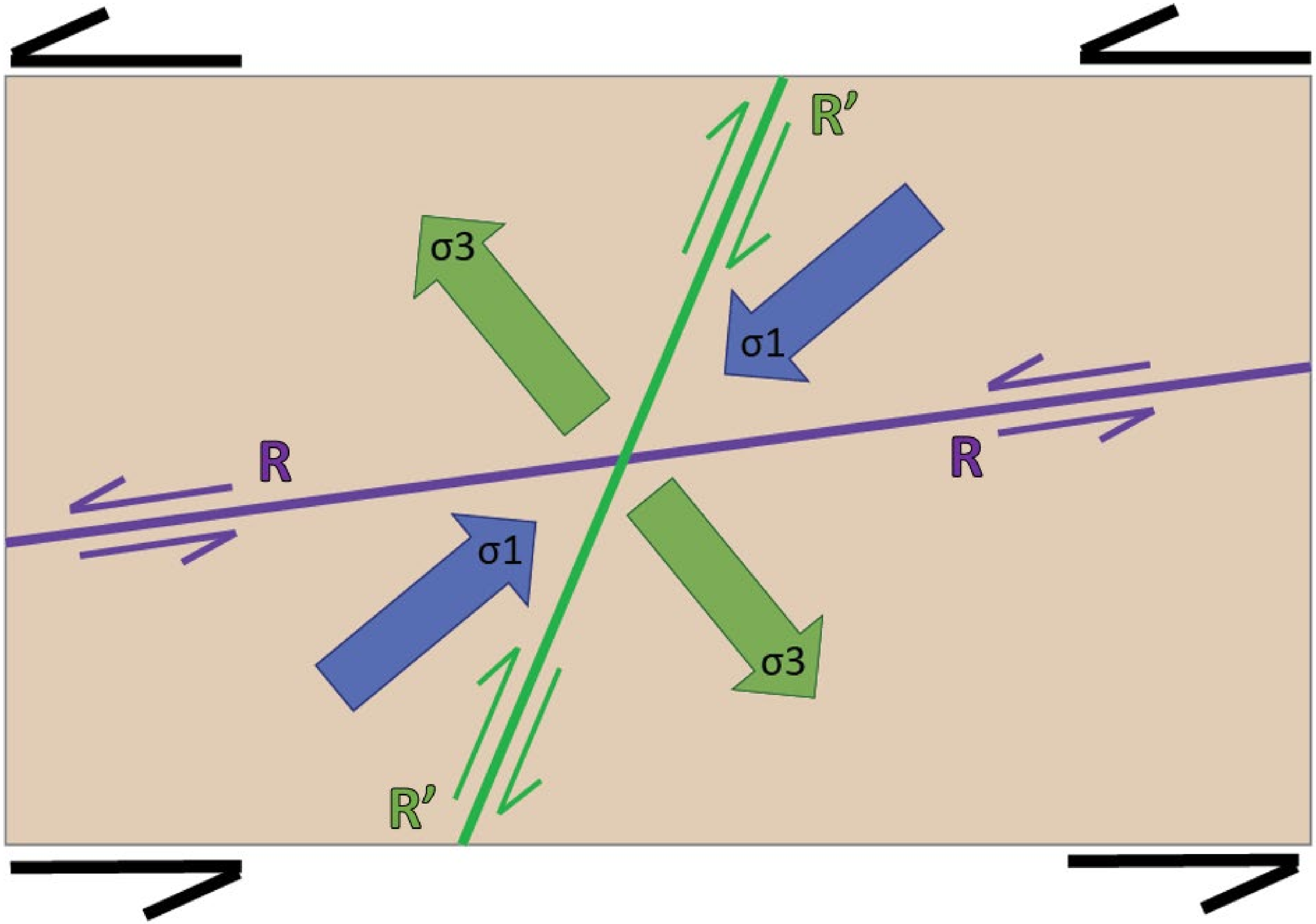

__Figure 22__ Schematic illustrating Riedel shears developing in a strike slip environment. In this example, extension (σ$_3$) occurs in an NW-SE direction, represented by the green arrows. The purple and green lines (R and R') are the faults and fractures formed under this stress regime. Magmatic constructs could exploit R and R'

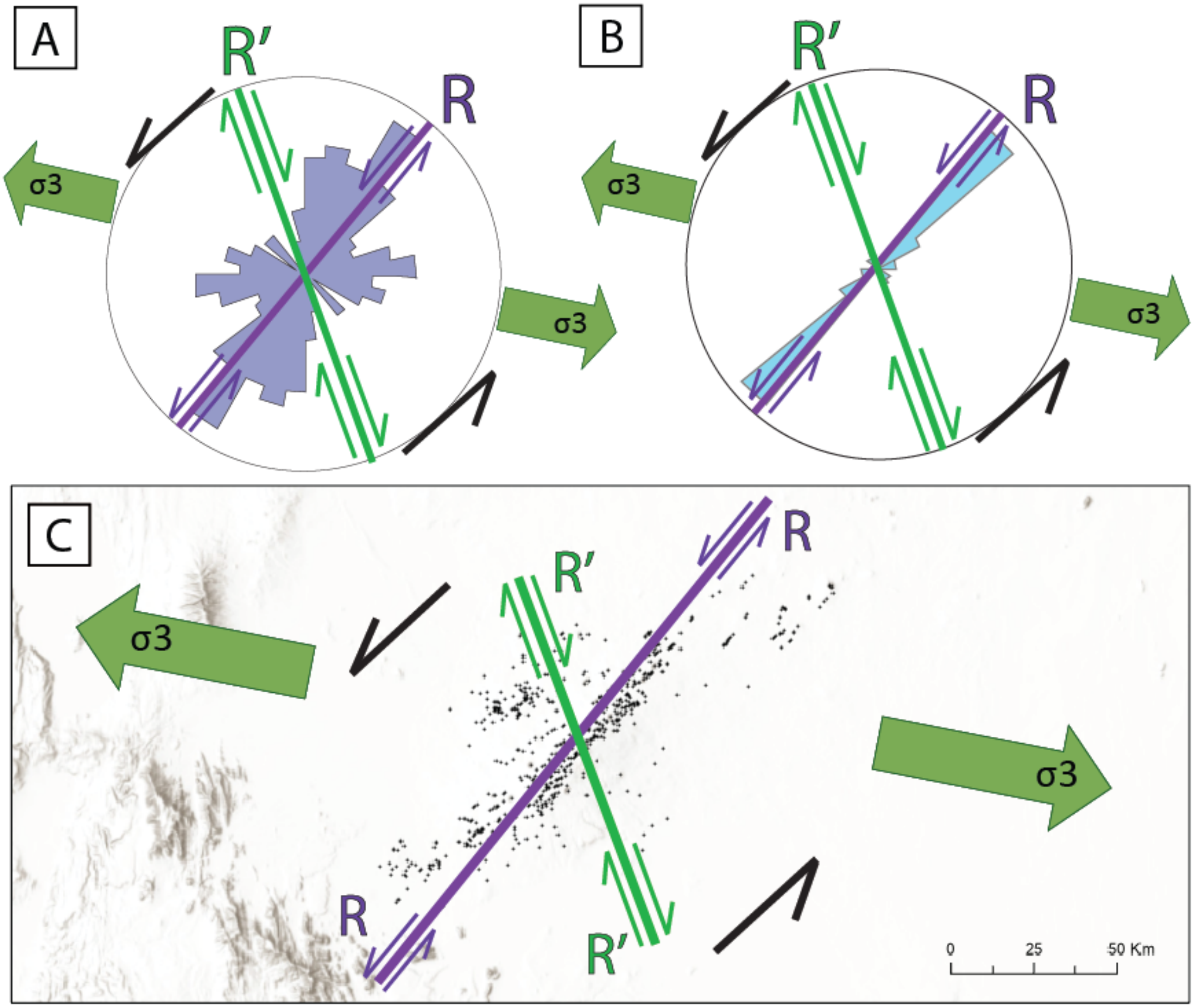

.

Figure 23 *Riedel shear schematics with an assumed WNW-ESE direction of extension.* A) *Rose diagram representing trends in the morphology of high confidence, elliptical volcanic centers. N = 185. The largest population is very close to R. B) Rose diagram representing trends in linear arrays identified using a width threshold of 10m and length threshold of 4,360m. N = 371. The primary population is also close to R. C) Terrain map of Marsabit. Black dots represent volcanic centers. The NE trending belts of features appear to be similar to R*

.

Appendices

Appendix A: ArcPy Code used to automate several processes in ArcGIS Pro for the morphology analysis.

Appendix B: Technical Walkthroughs

- B1- ArcGIS Pro- Set coordinate systems, upload KML, MBG, find center of polygons
- B2- MATLAB Dendrogram and NNd clusters
- B3- MATLAB 3-point Alignment Code
- B4- MATLAB KDE
- B5- EXCEL Identify KDE Peaks

Appendix C: A spreadsheet detailing volcanic centers on Mt Marsabit, including feature number, type, CL, UTM Coordinates, elevation, area, axis lengths, and long axis trends.

Appendix D: KMZ file of mapped features

Appendix E: Georeferenced map of all mapped volcanic features on Mt Marsabit

Appendix F: Results of the Poisson Nearest Neighbor Analysis

Appendix G: Rose diagrams of linear arrays within 25 different width and length combinations. The outer rim of the rose diagram has a value of 50%.

Appendix H: Spreadsheet with results of KDE analysis and best fit lines for linear arrays identified with the 3-point alignment code.